Bioactive Materials 47 (2025) 343–360

Contents lists available at ScienceDirect

Bioactive Materials

journal homepage: www.keaipublishing.com/en/journals/bioactive-materials

"Disguise strategy" to bacteria: A multifunctional hydrogel with bacteria-targeting and photothermal conversion properties for the repair of infectious bone defects

Kexin Li [a,1], En Xie [a,1], Chengyuan Liu [a], Jie Hu [a], Qianglong Chen [a], Jiaying Li [a], Huan Wang [a], Qingchen Meng [a], Dachuan Liu [a], Bin Meng [a], Ting Liang [a], Jinjin Ma [a], Zhangqin Yuan [a], Lijie Wang [d], Wenmiao Shu [c], Haijiao Mao [b], Fengxuan Han [a,**], Bin Li [a,*]

[a] Orthopedic Institute, Department of Orthopedic Surgery, Medical 3D Printing Center, The First Affiliated Hospital, MOE Key Laboratory of Geriatric Diseases and Immunology, School of Basic Medical Sciences, Suzhou Medical College, Soochow University, Suzhou, Jiangsu, 215000, PR China
[b] Department of Orthopaedic Surgery, The First Affiliated Hospital of Ningbo University, Ningbo, Zhejiang, 315020, PR China
[c] Department of Biomedical Engineering, University of Strathclyde, Glasgow, G1 1QE, UK
[d] Sanitation & Environment Technology Institute of Soochow University Ltd., Suzhou, Jiangsu, 215000, PR China

ARTICLE INFO

Keywords:
Bacteria-targeting
Antibacterial effect
Bone regeneration
Spatially controllable hydrogel
Infectious bone defect

ABSTRACT

Addressing the challenge of eliminating bacteria and stimulating osteogenesis in infectious bone defects, where cells and bacteria coexist within the microenvironment, presents a significant hurdle. In this study, a strategy of targeting bacteria is proposed to address this challenge. For this purpose, a methacrylated gelatin composite hydrogel containing zinc ion and D-type cysteine-modified polydopamine nanoparticles (PZC) is developed. The D-cysteine, involved in the metabolism of the bacterial peptidoglycan chain, allows PZC to specifically target bacteria, exhibiting a form of "disguise strategy". Through the targeting effect, this composite hydrogel can selectively kill bacteria and promote osteogenesis combing photothermal therapy with Zn^{2+} release, which showcases spatial controllability. Moreover, the antibacterial ability will be further improved after Near-infrared light irradiation. The multifunctional hydrogel containing Zn^{2+} modified nanoparticles can also promote osteogenic differentiation of bone marrow stem cells. Animal studies have revealed that the multifunctional hydrogel can inhibit bacteria growth and promote repair of infectious bone defects in rats. Findings from this study imply that endowing the nanoparticles with bacteria-targeting function can precisely control the events in cells and bacteria in the complex microenvironment, which can provide insights for the treatment of complex diseases with antibacterial requirements.

1. Introduction

Infectious bone defects, particularly those resulting from conditions like osteomyelitis, present significant challenges in terms of both infection control and bone regeneration. Current treatment strategies typically include a combination of antibiotics, surgical intervention, and bone grafts or scaffolds. The clinical treatment of infectious bone defects is highly challenging and can lead to serious complications, such as delayed bone healing and bone nonunion [1]. Further, open fractures are accompanied by severe bacterial contamination, and over 30 % develop osteomyelitis if not entirely and promptly debrided, thus imposing an enormous economic burden on patients [2]. To date, antibiotics are the primary clinical treatment method for infectious bone defects. However, the abuse of antibiotics can lead to uncontrolled infections, promoting the recurrence of infection and proliferation of drug-resistant bacteria, resulting in refractory infection [3]. Currently, there is a lack of suitable antibacterial materials for bone repair [4]. Therefore, the development of new treatment strategies is urgently

Peer review under the responsibility of KeAi Communications Co., Ltd.
* Corresponding author. Orthopedic Institute, Soochow University (North Campus), Ganjiang Rd 178, Suzhou, Jiangsu, 215000, PR China.
** Corresponding author. Orthopedic Institute, Soochow University (North Campus), Ganjiang Rd 178, Suzhou, Jiangsu, 215000, PR China.
E-mail addresses: fxhan@suda.edu.cn (F. Han), binli@suda.edu.cn (B. Li).
[1] These authors equally contributed to this study.

https://doi.org/10.1016/j.bioactmat.2025.02.002
Received 11 November 2024; Received in revised form 16 January 2025; Accepted 2 February 2025

needed.

Complete debridement, bone grafting or removal, and the use of systemic and local antibiotics are the foundation of traditional therapy for infectious bone defects. However, they show several disadvantages. The most common source of autogenous bone graft is pelvic, but the supply is limited [5]. Artificial bone substitutes may reduce the risk of medical complications, but they carry a significant risk of rejection and infection, and they lack antibacterial properties. Furthermore, most antibacterial materials effectively kill bacteria but can also damage normal cells [6]. In an effort to combine antibacterial and osteogenic capabilities, antimicrobial compounds such as antibiotics, silver (Ag), copper (Cu), and their oxides, as well as antimicrobial peptides, have been incorporated into osteogenic materials to enhance their antibacterial effectiveness [7–9]. These substances include polypeptides [10], polycaprolactone, poly (lactic-co-glycolic acid), polylactic acid [11], tricalcium phosphate [12], chitosan [13,14] and metal ions [15]. Despite their potent antibacterial properties, these materials have limitations, such as the potential toxicity of Ag, Cu, and their oxides. Additionally, the overuse of antibiotics has contributed to the development of drug resistance. Consequently, it remains challenging to find a single material that can effectively combine both antibacterial and osteogenic functions.

Photothermal therapy (PTT) represents an innovative strategy for destroying germs, particularly excelling in the fight against multidrug-resistant bacteria, with a reduced likelihood of developing resistance or causing systemic damage [16]. Near-infrared (NIR) light wavelength offers superior tissue penetration compared to other types of light. Normal biological tissues without photothermal agents suffer little heating effects when exposed to NIR in the 700–1300 nm range, which can penetrate tissues with great spatial and temporal accuracy. Therefore, PTT is outstanding as an emerging antibacterial strategy, owing to its ease of use and response to demand. In the context of bone defects, photothermal agents can convert NIR irradiation into heat, thereby eliminating bacteria through hyperthermia [17]. In addition to providing bacterial resistance, the ideal bone repair material should induce bone regeneration. The polydopamine (nanoparticles) NPs emerge as promising photothermal nanomaterials. They provide an excellent photothermal response to NIR irradiation and can easily connect with other materials via groups on the surface to achieve multifunctionalization [18]. A recent study revealed that polydopamine NPs were incorporated within biomaterials to enhance osteogenesis because they generated moderate photothermal stimulation (42–47 °C) [19]. However, the key to achieving controllable bacterial and cellular functions lies in the precise control of the spatial positioning of photothermal reagents. This control is fundamental to the effective and safe application of PTT in infectious bone defect treatment and bone regeneration.

The ability of bacteria-targeting holds great promise for the development of new antimicrobial materials [20,21]. These materials can employ various mechanisms such as covalent bonding, electrostatic attraction, receptor-ligand interactions, biomimetic alterations for bacterial capture, and micro/nanorobotics to target and eliminate bacteria in wounds or within deep organs. D-type amino acid (DAA), including D-type cysteine (D-Cys), can interfere with peptidoglycan chain metabolism. Previous studies revealed that fluorescence-labeled DAA can bind to the peptidoglycan chain for targeting and tracing the bacteria [22]. Additionally, DAA could inhibit the biofilm formation. Hence, they can be packaged into amphiphilic polypeptides and assembled into nanostructures for biofilm inhibition [23]. The biostability, biodistribution, and toxicity of supramolecular nanofibers may be regulated by the D-peptide, indicating that macromolecules embedded with DAA may display a range of biological functions [24]. Furthermore, cationic polypeptides have the ability to disrupt the negatively charged extracellular matrix of biofilms, offering a strategy to combat multidrug-resistant bacteria by disassembling their protective biofilms.

For infectious bone defects, both antibacterial activity and osteogenesis ability is critical. Previous studies revealed that Zn^{2+} exhibited antimicrobial and osteogenesis effects. Zinc is necessary for skeletal development, bone homeostasis, and cell function [25,26]. Zinc can improve chondrocyte and osteoblast functions while reducing osteoclast activity. Further, zinc uptake regulator protein regulates the virulence of bacteria. Bacterial intracellular accumulated Zn^{2+} would interact with the thiol group of bacterial respiratory enzymes, inhibiting their function [27]. Moreover, zinc is safer for normal cells compared to heavy ions. Additionally, zinc-based nanomaterials are easy to degrade metabolize in the body. Therefore, modifying zinc in the material is beneficial for both antibacterial and osteogenesis properties. A zinc finger typically refers to a protein domain that binds to zinc ions and facilitates protein-DNA interactions [28,29]. In the design of the hydrogel, zinc fingers could potentially be employed as binding sites for bacterial cell wall components or specific receptors on the bacterial surface. Zinc finger-inspired sequences or motifs can be incorporated into the hydrogel to specifically interact with bacterial surface proteins or receptors, such as lipopolysaccharides (LPS) on Gram-negative bacteria or teichoic acids on Gram-positive bacteria.

In this study, a strategy is developed to address the complex microenvironment of infectious bone defects by fabricating a multifunctional hydrogel with bacteria-targeting and photothermal conversion properties (Scheme 1). We develop a methacrylated gelatin (GelMA)/oxidized hyaluronic acid composite hydrogel (GO) containing zinc ion and D-Cys modified polydopamine (PZC) nanoparticles, wherein Zn^{2+} promotes osteogenesis and inhibits bacteria, whereas D-type cysteine targets bacteria. D-type cysteine modification is intended to help bacteria while simultaneously minimizing harm to host cells. The metabolism of bacterial peptidoglycan chains requires the involvement of D-amino acids. The surface of the PZC particles contains D-cysteine, which can serve as a substrate for bacterial peptidoglycan metabolism. Once the bacteria uptake the PZC particles as raw material, the particles can exert antibacterial effects by releasing zinc ions and generating photothermal effects under near-infrared (NIR) irradiation. These nanoparticles with bacteria-targeting components can gather in bacterial areas, thus avoiding excessive temperature rise and slowly release of Zn^{2+} in bone tissue cells. Further, the photothermal properties and Zn^{2+} release of the hydrogels are investigated. The in vitro and *in vivo* antibacterial performances of the hydrogels, including the bacteria-targeting ability of the NPs with or without NIR irradiation, are evaluated. The effect of the hydrogels on osteogenic differentiation of bone marrow stem cells (BMSCs) is studied. Further, a rat model of a femoral condylar infectious bone defect is used to evaluate the bone repair ability.

2. Results

2.1. Characterizations of the nanoparticles

The polydopamine (P) NPs were fabricated via self-polymerization in an alkaline environment, followed by stepwise modification of Zn^{2+} and D-Cys on their surface to obtain polydopamine-zinc ion (PZ) and polydopamine-zinc ion-D-type cysteine (PZC) NPs (Fig. 1A). The scanning electron microscopy (SEM) and transmission electron microscopy (TEM) images reveal that all the NPs are homogeneous and spherical (Fig. 1B and C). Zeta potential analysis shows that all the NPs are negative charged (Fig. 1D), and the average diameter of P, PZ, and PZC is 93 ± 14, 92 ± 23 and 104 ± 28 nm, respectively (Fig. 1E–G).

Energy-dispersive X-ray (EDX) analysis reveals that P NPs contain carbon, nitrogen, and oxygen elements. In contrast, PZ comprises zinc, indicating successful modification of Zn^{2+} on the NP surface. For PZC, sulfur is detected, indicating the successful modification of D-Cys on the PZC surface (Fig. 2A). The Fourier transform infrared (FTIR) spectra shows that the peak disappears at 3294 cm^{-1} in PZ, demonstrating the disappearance of the phenolic hydroxyl group due to the coordination with Zn^{2+}. The appearance of a peak at 844 cm^{-1} in the PZC is attributed to the C-S bond vibrations of D-Cys, thus confirming the successful modification of D-Cys to the PZ particle (Fig. 2B). Further, the solutions

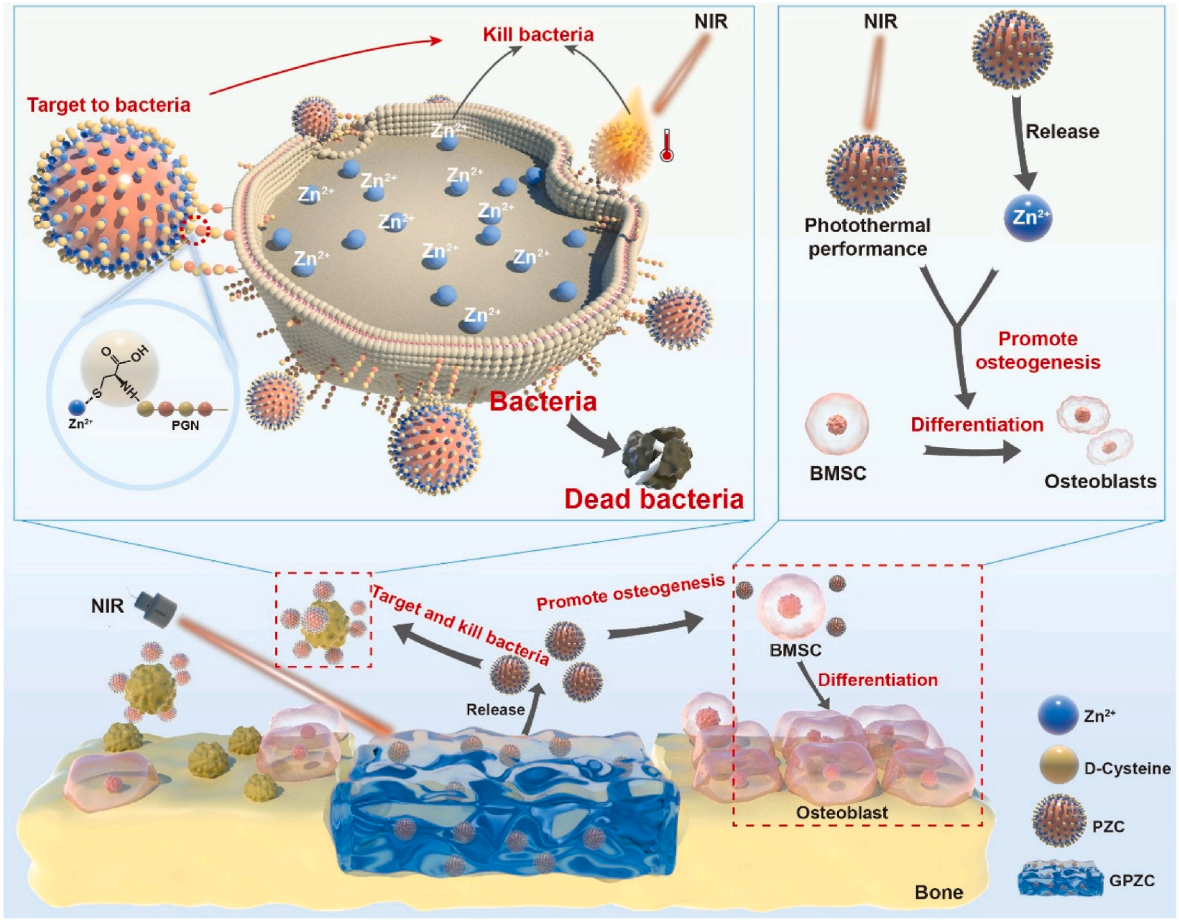

Scheme 1. Schematic depiction of the strategy of bacteria-targeting to address the complex microenvironment of infectious bone defects by a multifunctional hydrogel.

with various concentrations of PZC were irradiated by 980 nm laser emitter for 10 min (1.0 W/cm^2), and display different maximum temperatures of 37.0 °C, 40.0 °C, 52.0 °C, 54.2 °C, and 55.4 °C, respectively (Fig. 2C). Laser penetration investigations frequently employ chicken breast muscle because of its homogeneity and low fat content. Significantly higher temperatures were observed under 980 nm laser irradiation (1 W/cm^2) (Fig. S1). The 980 nm laser was able to penetrate a thicker layer of chicken breast muscle (estimated at 3.3 mm) when PZC was heated to 42 °C.

2.2. Characterizations of the composite hydrogels

The aldehyde group of GelMA-OHA (GO) and the amino group of P NPs form Schiff base, which breaks in an acidic environment. The P, PZ, and PZC NPs were added into GO, to prepare GP, GPZ, and GPZC hydrogels, respectively (Fig. 3A). The SEM images reveal that the hydrogels have loose porous structure, which is necessary for cell growth and migration (Fig. 3B). The photothermal properties of GP, GPZ, and GPZC hydrogels containing different NPs (200 mg/mL) were investigated at different temperatures (25.6 °C, 42.3 °C, 44.5 °C and 46.6 °C) (Fig. 3C–S2). Further, during three times of "on/off" cycling experiments, all groups maintain similar temperature changes, demonstrating good stability of the materials (Fig. 3D). Subsequently, P NPs were added to the GelMA to obtain a composite hydrogel with varying particle amounts. The mechanical test results reveal that Young's modulus and strength of the hydrogels decrease after loading P, PZ, and PZC (Fig. 3E–G), owing to the incorporation of NPs which hinders the GelMA chemical cross-linking. However, the composite hydrogels can release Zn^{2+} and D-cys faster in the acidic environment (Fig. 3H–J). After 21 days, the cumulative release of Zn^{2+} in PBS at pH 5.5 is 33.7 ± 1.1 μmol/L, whereas that at pH 7.2 is 27.9 ± 1.1 μmol/L. Zn^{2+} can be released faster due to the breaking of Schiff base bond in the acidic microenvironment. PZC NPs modified with D-Cys result in a lower release from the GPZ hydrogel than that from GPZ, with values of 29.5 ± 0.6 and 23.3 ± 1.3 μmol/L in PBS at pH 5.5 and 7.4, respectively. We implanted the composite hydrogel subcutaneously in rats to observe *in vivo* degradation (Figs. S3 and 4). The GPZC hydrogel degrades faster compared to the GO hydrogel without particles. On day 14, the mass of the GPZC hydrogel was 30.7 % of its original mass, which could achieve a long-term, slow release in the body.

2.3. Biocompatibility of the hydrogels

To assess the biocompatibility of GP, GPZ and GPZC, cytoskeleton staining of BMSCs was performed after 48 h co-culture (Fig. 4A and B). Good cell growth is observed on GPZC at 0, 1, and 2 mg/mL concentrations of PZC, whereas no cells are observed at 4 mg/mL. Consequently, the composite hydrogel containing 2 mg/mL PZC NPs is chosen for the following study. The images of cytoskeleton staining indicate that cells in GP, GPZ, and GPZC groups have more filamentous pseudopods and mature actin stress fibers. The CCK-8 results exhibit a similar trend (Fig. 4C and D). The live/dead staining results reveal that NIR irradiation has little effect on the proliferation and activity of BMSCs, suggesting that the experimental parameters of photothermal treatment in this study are appropriate (Fig. 4E). The effect of NIR light exposure on cell viability was evaluated by CCK-8 assay (Fig. S5). The results showed no significant difference in OD values between the GPZC+ and Ctrl groups, indicating that NIR exposure for up to 15 min didn't affect cell

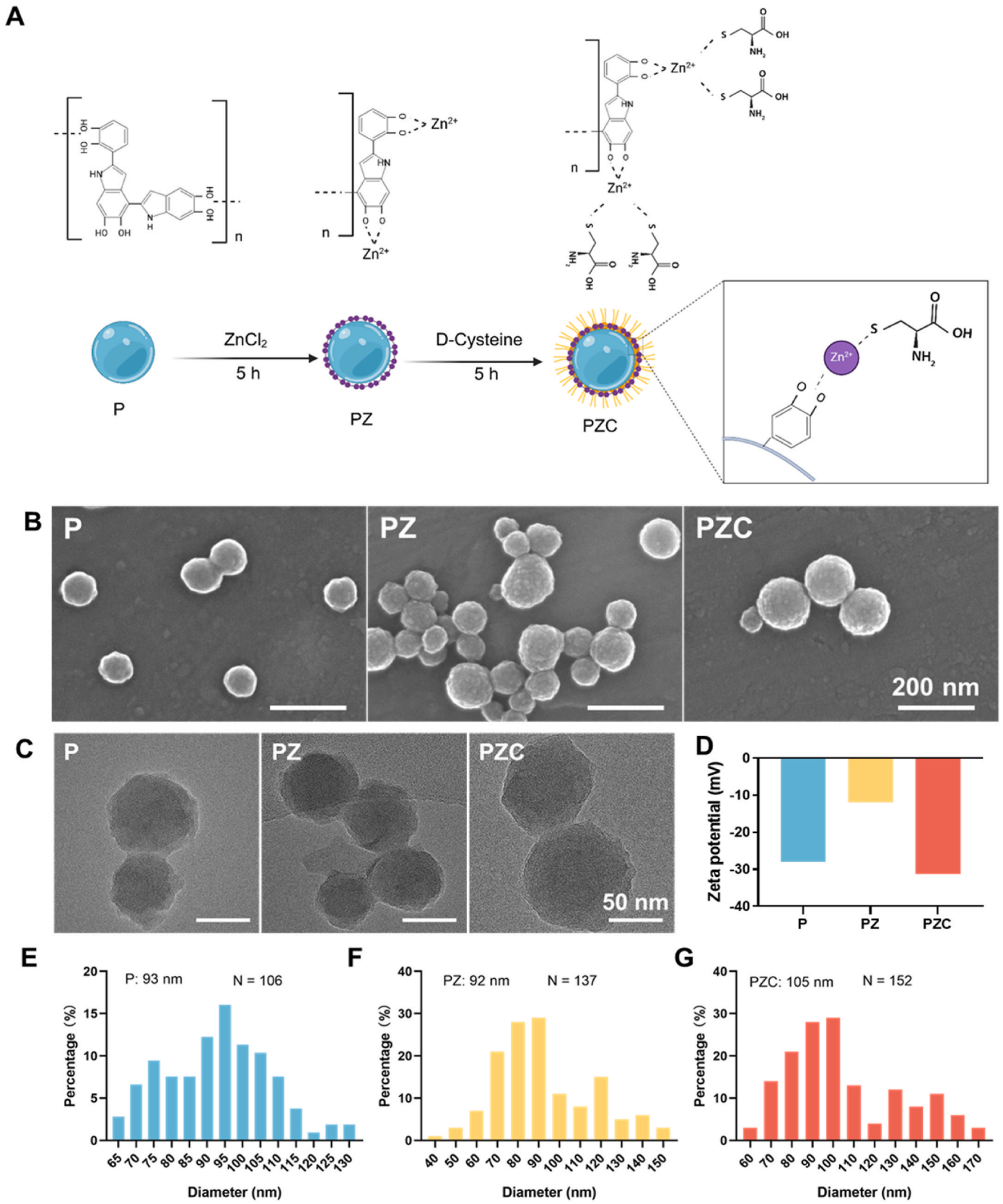

Fig. 1. Characterizations of the NPs. (A) Synthesis progress of PZC. (B) SEM images of P, PZ, and PZC. (C) TEM images and (D) zeta potentials of P, PZ and PZC. (E–G) Diameter distribution of P, PZ and PZC, respectively.

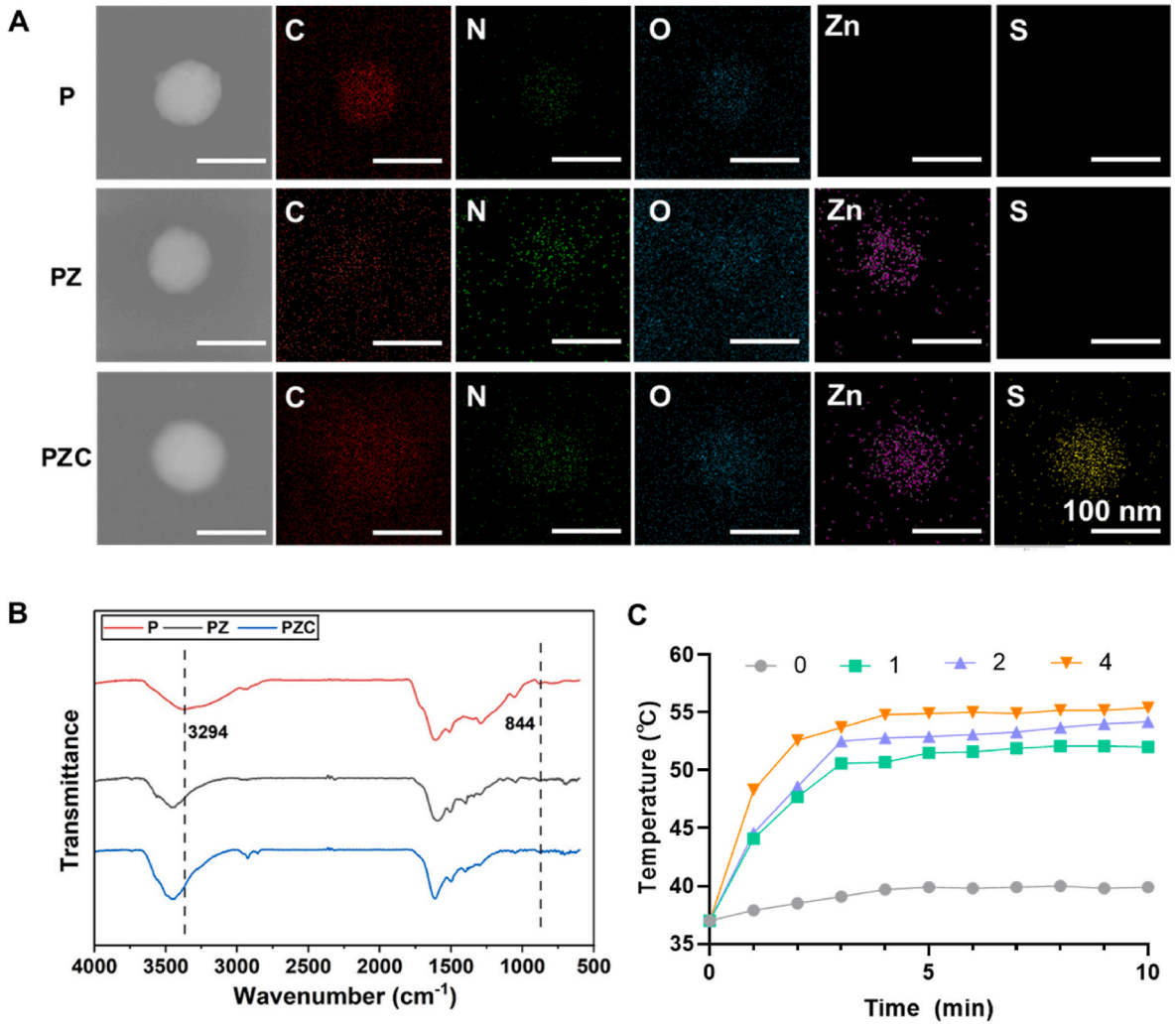

Fig. 2. Characterizations of NPs. (A) Elemental mapping analysis of P, PZ and PZC. (B) FTIR spectra of P (green), PZ (red) and PZC (blue). (C) Temperature-elevating curves of PZC at 0, 1, 2 and 4 mg/mL concentrations under NIR irradiation in PBS.

viability.

2.4. In vitro antibacterial properties

The growth of *Staphylococcus aureus* (*S. aureus*) on the composite hydrogel surface was observed via AO/EB staining (Fig. S6). A large number of live bacteria (green) are observed on the hydrogel surface without 980 nm NIR treatment. Further, the GPZ and GPZC groups have a large number of dead bacteria (red) owing to the release of Zn^{2+}. With 980 nm NIR light irradiation at 1 W/cm^2, the GP$^+$, GPZ+, and GPZC + groups achieve superior bactericidal effects owing to the photothermal conversion properties. The antimicrobial effects of the GPZ+ and GPZC + groups are obvious due to the simultaneous release of Zn^{2+}. The GP, GPZ, and GPZC groups show no antibacterial activity in the absence of NIR irradiation. However, upon NIR irradiation (980 nm, 1.0 W/cm^2), their antibacterial abilities improve considerably owing to the photothermal effect (<50 °C). Further, SEM images reveal that some *S. aureus* grow on GP, GPZ, and GPZC. However, fewer bacteria adhere to GPZ and GPZC surfaces after NIR irradiation, and the bacteria deform due to heat and Zn^{2+} (Fig. 5A). The inhibitory zone experiment demonstrates that the distance without bacterial colonies for the GPZC hydrogel is approximately 3 mm, considerably greater than that of GO (Fig. 5B). The antibacterial rates of *S. aureus* colonies on the GPZ and GPZC hydrogels at 980 nm NIR radiation are 97.7 and 96.4 %, whereas those on GO and GP composite hydrogels are approximately 34.8 and 83.2 %, respectively (Fig. 5C and D). Moreover, the antibacterial kinetics of composite hydrogels was studied. Fig. S7 shows that GPZC with NIR irradiation rapidly eradicates living bacteria, and the bacterial killing activity is time-dependent. We further evaluated the inhibitory effect of the materials on biofilm formation (Fig. 5E and F). The GPZ and GPZC under NIR irradiation could inhibit biofilm formation. We included a gentamicin -releasing hydrogel as a positive control at clinically relevant concentrations (Fig. S8). The results show that both G-Gentamicin and GPZC + NIR exhibit comparable efficacy, suggesting that GPZC + NIR could be a promising alternative to current antibiotic-only treatments, addressing issues such as resistance and tissue toxicity.

2.5. The bacteria-targeting ability of PZC

BMSCs, *S. aureus,* and PZC were labeled with DiO perchlorate (green), DiI perchlorate (red), and Cy5 (blue), respectively. The results show that after co-culturing the BMSCs (green) and *S. aureus* (red) for 12 h, more PZC particles (blue) concentrate on the area of *S. aureus*, indicating that PZC exhibits good bacteria-targeting ability (Fig. 5G). We also conducted the co-culture experiment involving cells, particles and *S. aureus* and *Escherichia coli* (*E. coli*) at 6 and 12 h (Fig. S9). *S. aureus* and *E. coli* were selected as representatives of different bacterial species, and 6 h and 12 h were set for dynamic observation of the targeting behavior of PZC particles. According to the fluorescence imaging results, PZC particles were able to target the bacteria after 6 h of co-culture, and

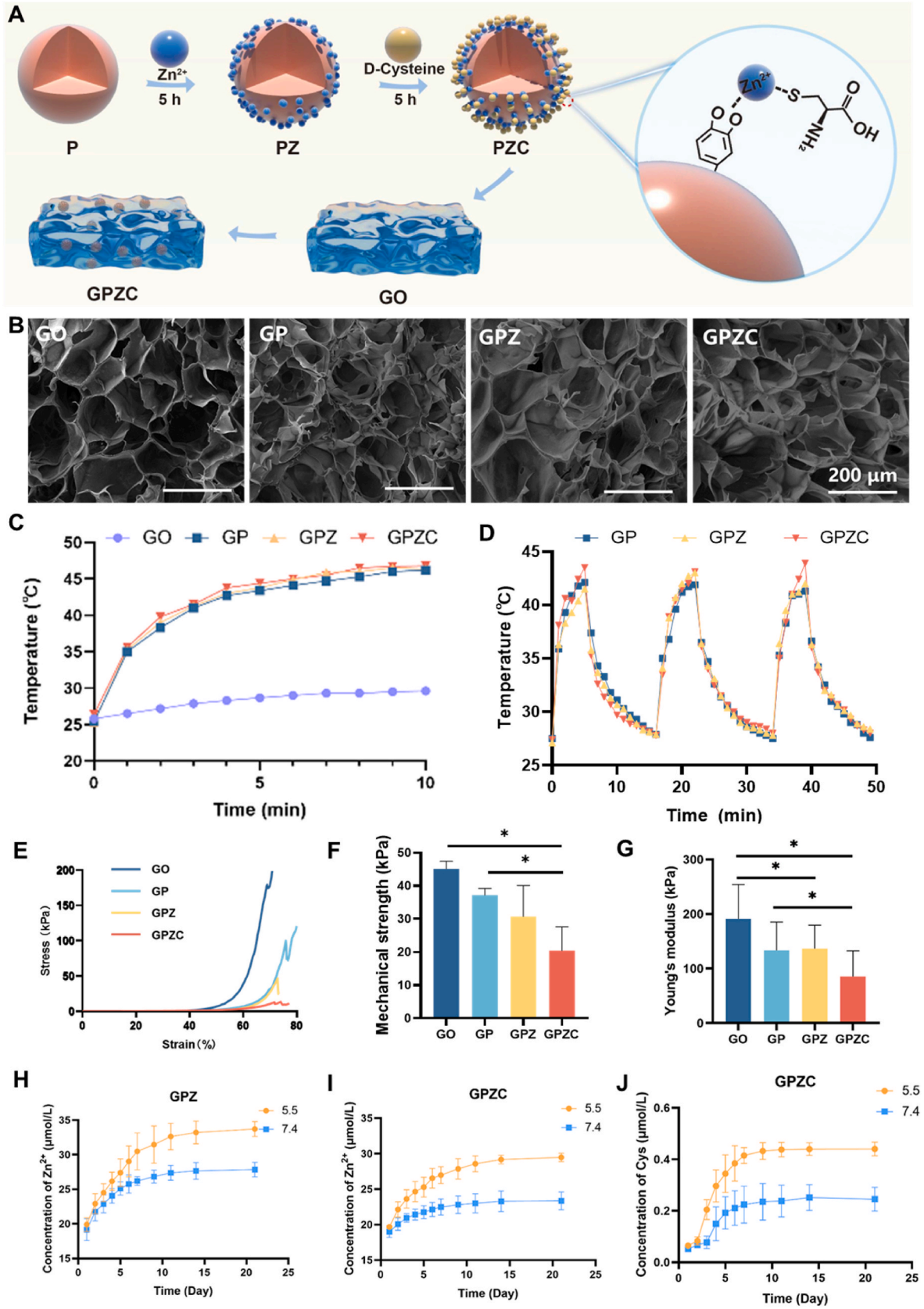

Fig. 3. Characterizations of the hydrogels. (A) Schematic diagram of preparation process of GPZC. (B) SEM images of the GO, GP, GPZ and GPZC. (C) Temperature-elevating curves of GO, GP, GPZ and GPZC under NIR irradiation. (D) Cyclic heating profiles of GP, GPZ and GPZC for three on/off cycles in PBS (laser on: 6 min laser off: 10 min). (E–G) Mechanical properties of the composite hydrogels. The concentration of Zn^{2+} released from (H) GPZ and (I) GPZC. (J) The release behavior of D-Cys from GPZC. (*, $p < 0.05$).

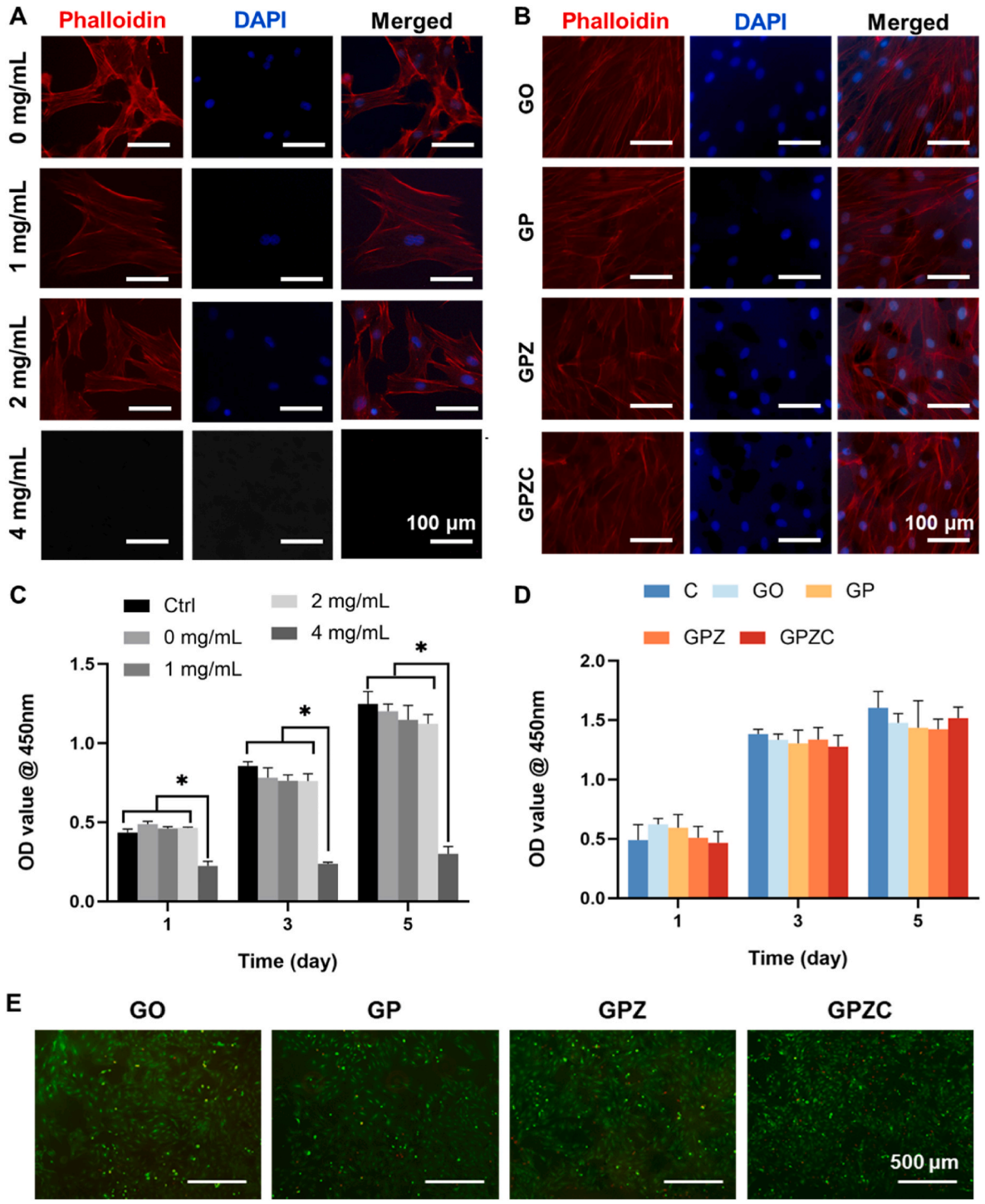

Fig. 4. Biocompatibility of the hydrogels. (A) Fluorescent images of BMSCs on the GPZC. (B) Fluorescent images of BMSCs on GO, GP, GPZ and GPZC. (C) CCK-8 assay of cells cultured with GPZC at different concentrations for 1, 3 and 5 days (D) CCK-8 assay of cells cultured with GO, GP, GPZ and GPZC. (E) Live/dead staining. (*, $p < 0.05$).

targeting was observed for both bacterial species.

2.6. *In vitro* osteogenesis ability

Alkaline phosphatase (ALP) plays a critical role in the bone mineralization process by binding to bone matrix proteins and stimulating pyrophosphate hydrolysis, making it a renowned biomarker for osteogenesis. For ALP, the expression of different groups follows the order of GPZC+ > GPZ+ >other groups after incubation for 7 days (Fig. 6A). The Alizarin red S (ARS) staining results show that GP+, GPZ+, and GPZC + induce more mineralized extracellular matrix and exhibit superior osteogenic differentiation property compared to those of the control, GP, GPZ, and GPZC groups (Fig. 6B), which is further illustrated by the quantitative analysis (Fig. 6C). The relative expressions of osteogenic differentiation protein and genes in BMSCs are shown in Fig. 6D and E. The *Alpl* and *Bglap* expressions of BMSCs in GPZ and GPZC with NIR irradiation are remarkably higher than those in the control group and the groups without NIR irradiation, indicating stronger osteogenesis

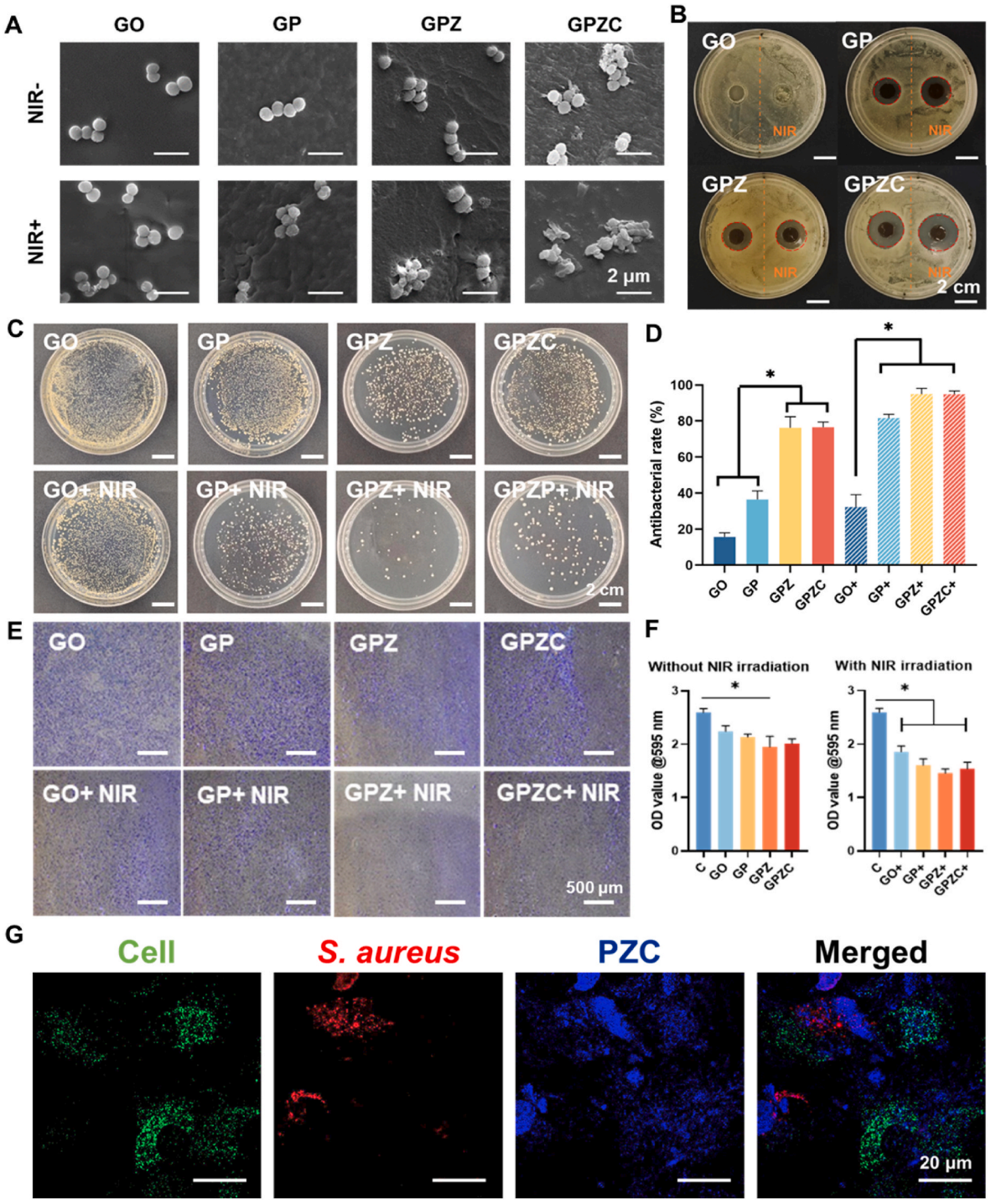

Fig. 5. *In vitro* antibacterial effects of different hydrogels. (A) SEM images of bacteria on different hydrogels with/without NIR irradiation. (B) The inhibition zone on the LB culture plates with *S. aureus*. (C) Optical images of *S. aureus* colonies formed on LB culture plates. (D) Antibacterial efficiency of the hydrogels with/without NIR irradiation. (E, F) Bacterial biofilm inhibition ability. (G) The bateria-targeting ability of PZC. (*, $p < 0.05$).

ability of GPZ+ and GPZC + groups. Additionally, the GPZ+ and GPZC + have remarkably higher *Col1a1* and *Runx2* expressions than those of the control group, indicating that GPZ+ and GPZC + enhanced osteogenic differentiation of BMSCs. We induced an in vitro inflammatory environment by LPS to investigate the osteogenesis potential of GPZC hydrogel under inflammatory conditions. Based on the results of ALP and ARS staining, the GPZC hydrogel exhibited promising osteogenesis effects under 980 nm NIR irradiation (Figs. S10–11). The results of Western blot showed that the expression of TNF-α in BMSCs treated with GPZC and 980 nm NIR was significantly lower compared to BMSCs treated with LPS alone, indicating that the GPZC hydrogel combined with 980 nm NIR exhibits a strong anti-inflammatory effect (Fig. S12). We also investigated the relationship between heat shock proteins and the osteogenesis pathway (Figs. S13–14). After NIR irradiation, BMSCs in the GPZC hydrogel group showed a significant increase in HSP70 expression, along with a notable upregulation of *Bmp*2 gene expression.

2.7. *In vivo antibacterial capability*

The infected femoral defect model was established, and *in vivo*

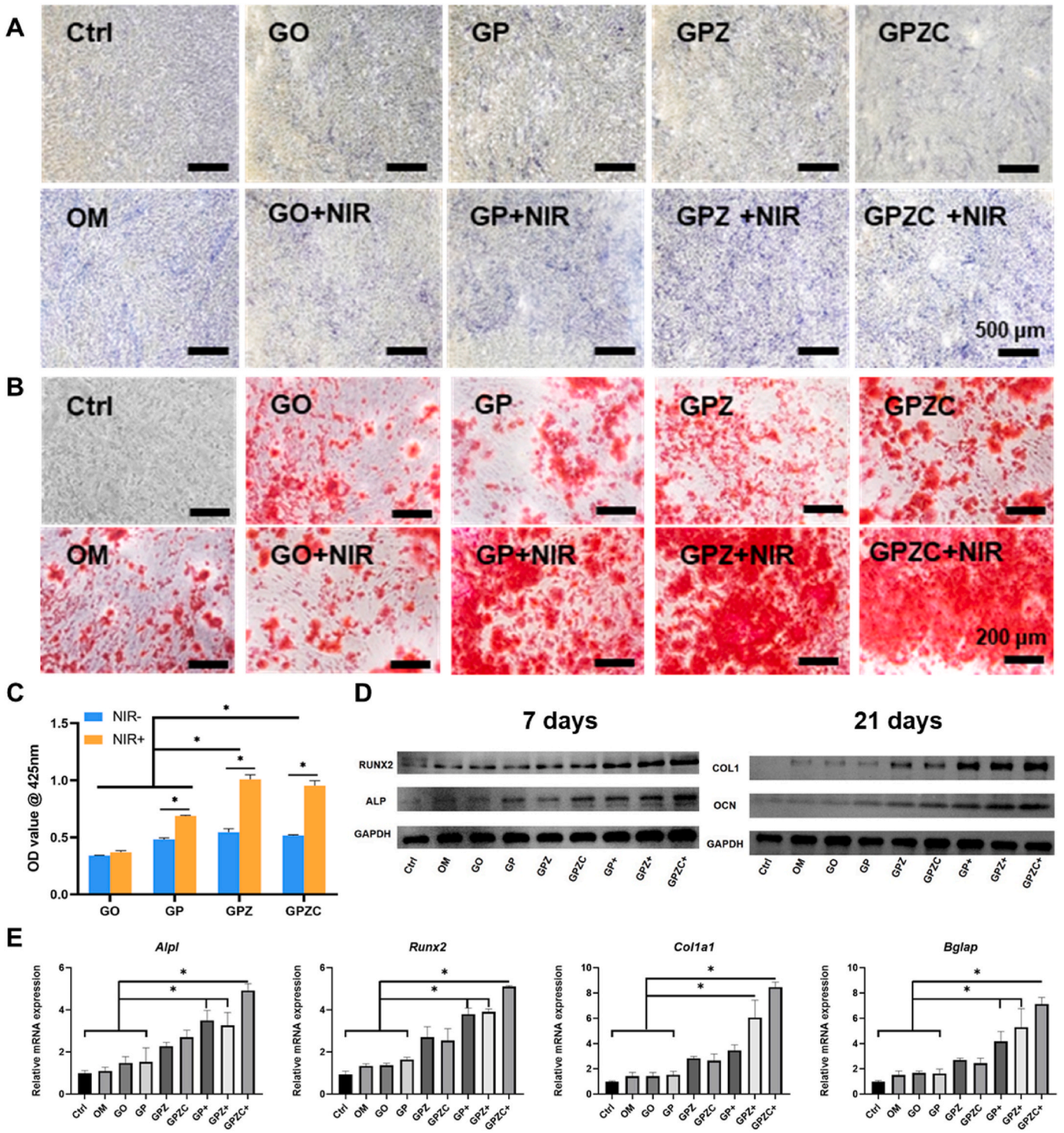

Fig. 6. *In vitro* osteogenesis ability. (A) ALP and (B) ARS staining of BMSCs cultured on different hydrogels at 7 and 21 days, respectively. (C) Quantitative analysis of extracellular matrix mineralization. (D) Western blot analysis of osteogenesis-related protein expression of BMSCs. (E) The expression of osteogenesis-related genes at 7 and 21 days. (*, $p < 0.05$).

antibacterial properties and pro-osteogenesis of composite hydrogels under NIR irradiation were studied. The temperature of the implanted GP+, GPZ+, and GPZC + increases from 36.2 to 45.0 °C within 120 s under 1.0 W/cm^2 NIR irradiation. After 7 and 14 days post-implantation, three rats from each group are used to evaluate the antibacterial properties. The colony count results reveal that GP+, GPZ+, GPZC+, and GPZC- groups show antibacterial efficiencies of 77.3 ± 6.5, 92.3 ± 8.9, 98.3 ± 0.4, and 57.5 ± 15.0 %, respectively (Fig. 7A and B). Secretions and pus are visually detected at the implant site of the defect group, which are partially diminished in the GPZC group. In contrast, the GPZ and GPZC groups after NIR irradiation are free from secretion and pus, indicating the eradication of bacterial infection. Fluorescence staining images of *S. aureus* depict the same tendency. The defect group has strong green fluorescence and the GPZC group with NIR irradiation has no green fluorescence, demonstrating its excellent *in vivo* antibacterial efficacy (Fig. S15). Compared to other groups, the expression of IL-

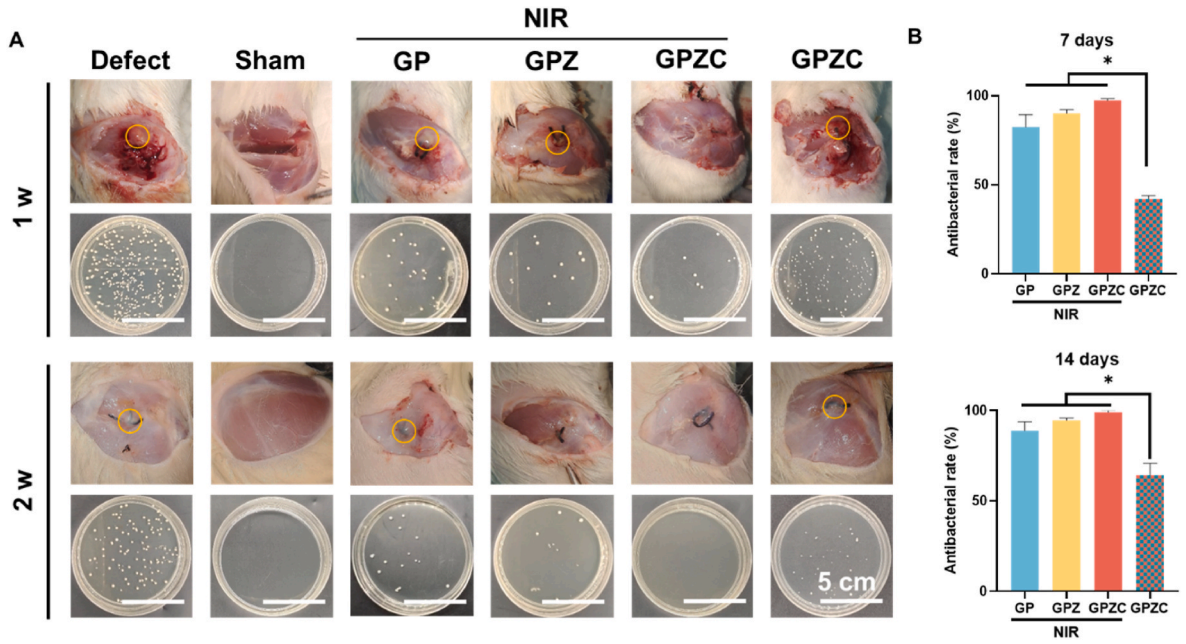

Fig. 7. Antibacterial activity of the hydrogels in infectious bone defects. (A) The images of infected femoral condyles and *S. aureus* colonies on LB culture plates and (B) quantitative analysis. (*, $p < 0.05$).

1β in the GPZ and GPZC groups after NIR irradiation was significantly lower, indicating that the GPZC hydrogel exhibits good anti-inflammatory effects under 980 nm NIR exposure (Fig. S16). We implanted the hydrogel subcutaneously in rats to observe its immunological effects on the surrounding tissues (Fig. S17). According to the H&E staining and immunohistochemical results, the expression of IL-1β in the surrounding skin tissue of the GPZC hydrogel group was lower than that in the GO group, and fewer neutrophils were observed. Hence, the GPZC group with NIR irradiation exhibits the best *in vivo* antibacterial capacity owing to the synergistic effects of photothermal therapy, Zn^{2+} and bateria-targeting ability.

2.8. Bone repair ability of different hydrogels in infectious bone defects of rats

GP, GPZ, and GPZC were implanted into the infectious femoral condyles defects of rats to assess the bone repair ability of the hydrogels (Fig. 8A). At 4 weeks, the Defect group still has a large void, and the defects of GP + NIR, GPZ + NIR, and GPZC are smaller but visible (Fig. 8B). However, the GPZC + NIR group is mostly healed, and only a small void was observed. After 8 weeks, the defects in the Defect group are evident. However, the GP + NIR, GPZ + NIR, GPZC + NIR, and GPZC- groups are repaired to varying degrees. Micro-computed tomography (Micro-CT) was used to analyze new bone formation, and the results are shown in Fig. 8C. No obvious new bone formation is observed in the Defect and GPZC groups at 4 weeks, whereas substantial new bone formation occurs at the edges in the GP, GPZ, and GPZC groups with NIR irradiation. At 8 weeks, new bone formation occurs around the edges in all groups, and the GPZC + NIR group exhibits the best bone repair ability.

The quantitative analyses of micro-CT show that the GPZ and GPZC groups undergoing NIR treatment remarkably enhance the bone mineral density (BMD), new bone volume (BV), and new bone volume to total tissue volume (BV/TV) in the femoral condylar defect at 4 and 8 weeks (Fig. 9A). The quantities of bone formation and anabolism are substantially higher in the GPZ and GPZC groups with NIR irradiation than those in the Defect, GPZC, and GP groups with NIR irradiation. Fig. 9B shows new bone formation in the control, GP+, and GPZC- groups at four weeks, which implys no considerable improvement in the defects. In contrast, the GPZC + group shows a considerable amount of new bone formation at the edge of the defects in all groups. The results of the GPZ and GPZC groups with NIR irradiation show more newly formed bone, suggesting that the GPZ and GPZC hydrogels undergoing NIR treatment promote bone regeneration (Fig. 9B and C). Therefore, the GPZC with NIR treatment could be used as a repair material for infectious bone defects.

2.9. Angiogenesis ability

To validate the angiogenesis potential of the hydrogel, we performed CD31 immunohistochemical staining of bone tissue sections, scratch assays, and tube formation assays (Figs. S18–20). The CD31 immunohistochemical staining results indicated that no significant differences were observed in CD31 expression between different groups. The results from the scratch assay and tube formation assay showed the GPZC hydrogel combined with NIR irradiation promotes angiogenesis.

2.10. In vivo biosafety of the hydrogels

The *in vivo* investigation of short-term biosafety was carried out. To assess the inflammatory response of the host, H&E staining was employed. The morphological characteristics of each organ tissue are evidently shown by the H&E staining findings (Fig. 10). In these organs of the rats implanted with the GPZC receiving NIR radiation, there are no obvious pathological alterations or histomorphological abnormalities. Additionally, both side effects and acute pathological systemic toxicity are not observed. These results suggest that the GPZC group with NIR irradiation exhibits excellent *in vivo* biosafety.

3. Discussion

Infectious bone defects are characterized by the coexistence of infection and bone injury, presenting serious complications such as nonunion, which imposes a significant burden on society. Antibiotics are the cornerstone of treating bone infections. Broad-spectrum antibiotics or specific drugs are commonly used. Over time, bacteria can develop resistance to commonly used antibiotics, further reducing the effectiveness of treatment and leading to persistent or recurrent infections.

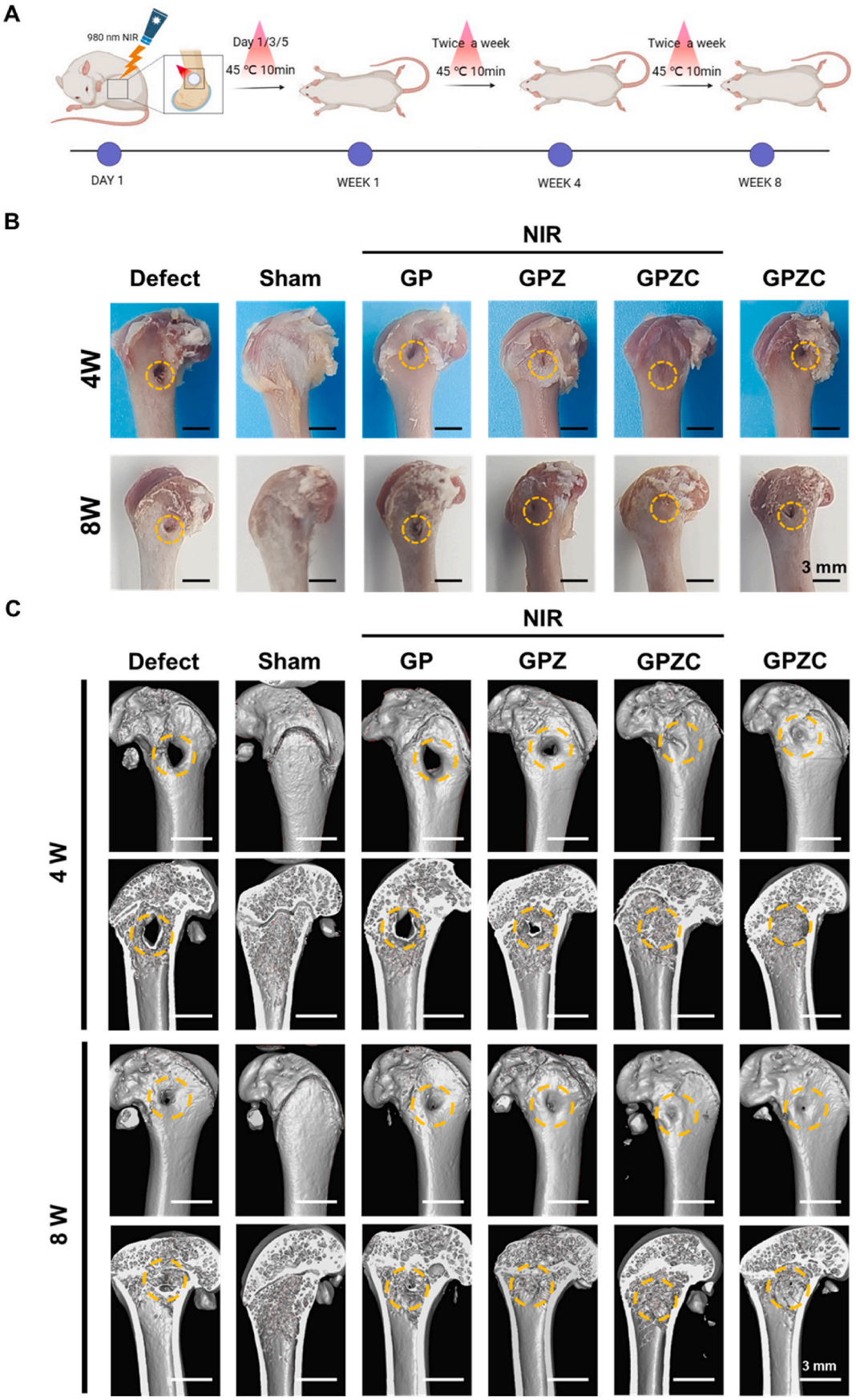

Fig. 8. Bone repair of the hydrogels in infectious bone defects. (A) Schematic diagram of model construction and treatment of infectious femoral defects in SD rats. (B) Macroscopic photos of the femur implanted with different hydrogels at 4 and 8 weeks. (C) Reconstructed images of micro-CT.

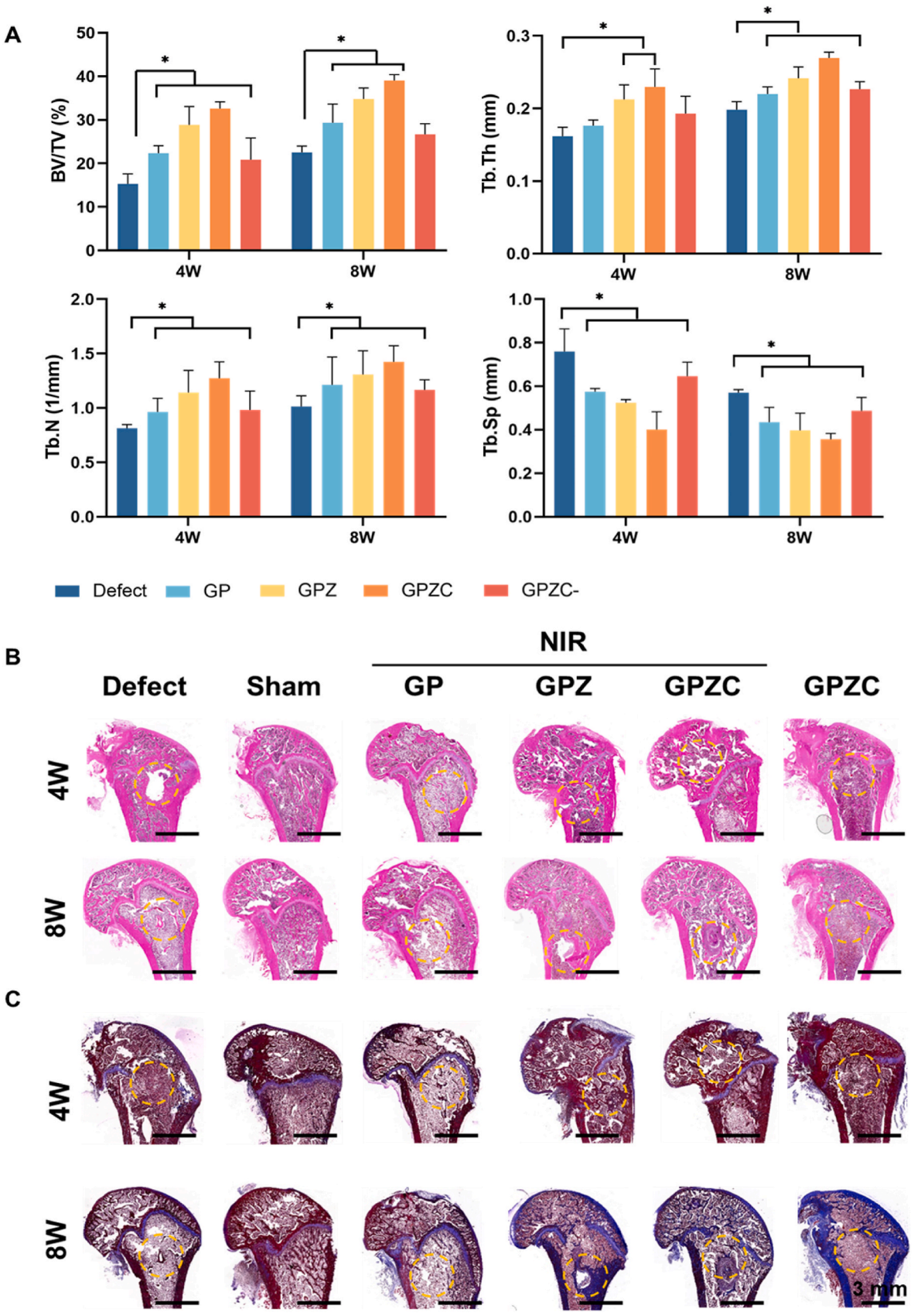

Fig. 9. Bone repair of the hydrogels in infectious bone defects of rats. (A) Quantification of BV/TV, trabecular bone number (Tb.N), trabecular thickness (Tb.Th), and trabecular space (Tb.Sp) of the micro-CT data. The images of (B) H&E and (C) Masson staining. (*, $p < 0.05$).

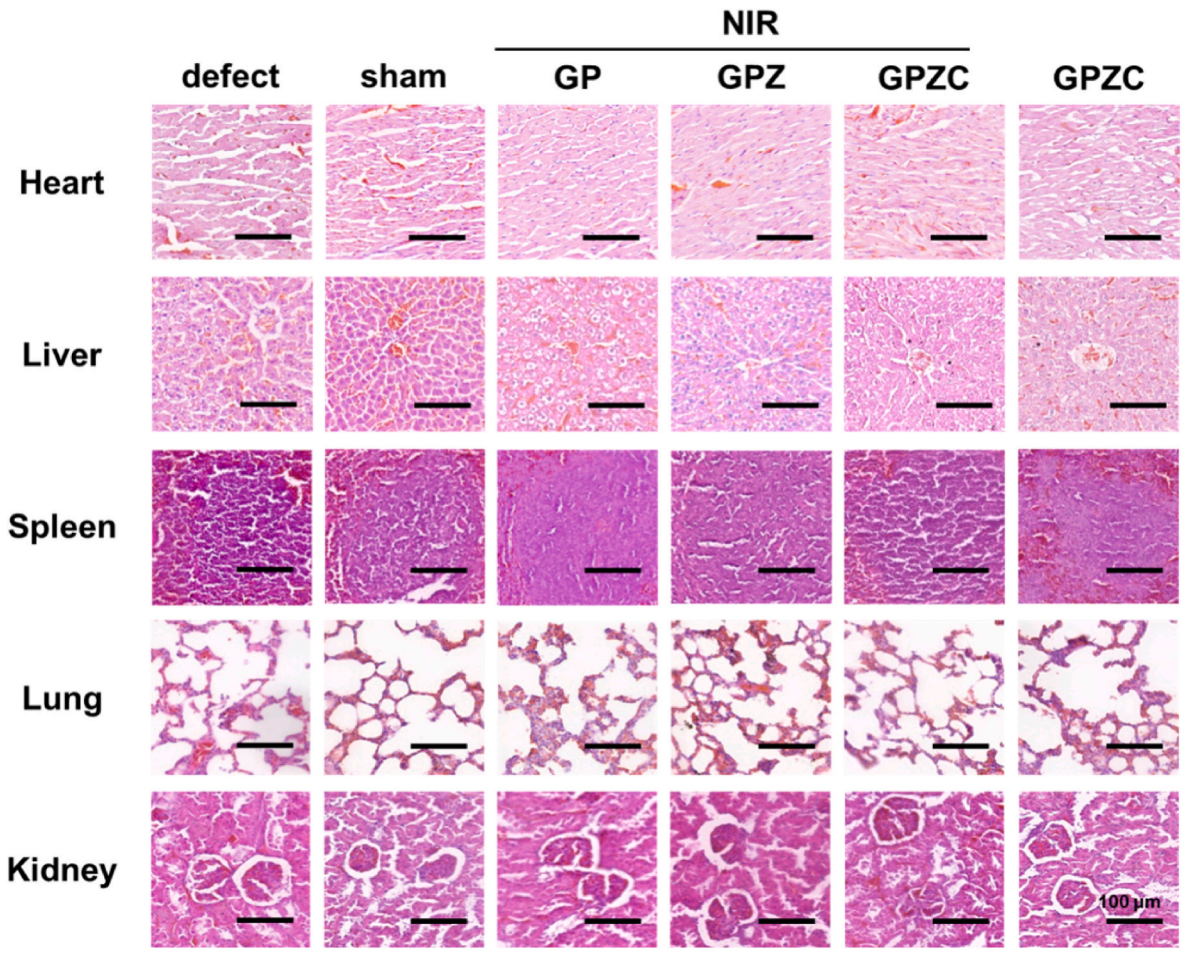

Fig. 10. Histological evaluation of heart, liver, spleen, lung and kidney of SD rats treated with different hydrogels at 4 weeks.

Prolonged use of antibiotics can lead to systemic side effects, including gastrointestinal issues, renal toxicity, or alterations in the microbiome, which can hinder health and recovery. Surgical debridement involves the removal of infected tissue, bone fragments, and foreign bodies to reduce the bacterial load. Surgical intervention is invasive and carries risks of complications such as bleeding, infection, or damage to surrounding tissues. Even after debridement, infections can recur, especially if the antibiotic therapy is not effective or if biofilms persist in the bone. In cases of large bone defects, bone grafting or scaffolding alone may not be sufficient for proper bone healing, and there may be issues with graft rejection, non-union, or incomplete healing. Bone grafts, either autografts, allografts or synthetic scaffolds, are used to fill defects and promote new bone growth. If the bone grafts or scaffolds become infected, they can be very difficult to treat, and removal or replacement may be required, which increases patient morbidity. In addition, in infectious microenvironment, the implanted grafts don't always support adequate bone regeneration in large defects, and there is a risk of non-union or graft failure. With the development of regenerative medicine, nanomaterials have been widely used for bone tissue engineering, ranging from stem cell regulation to bone repair. However, the key challenge lies in achieving bone regeneration and bacterial eradication without harming normal cells [30,31].

Therefore, photothermal conversion materials have been used to kill bacteria through photothermal action. PTT utilizes converting light into heat energy by photothermal conversion materials (e.g., metallic nanoparticles, two-dimensional nanomaterials, and organic materials) to disrupt the integrity of pathogenic bacterium, leading to leakage of bacterial contents, thereby showing killing effect [32–35]. This heat-dependent killing effect does not lead to bacterial resistance owing to its different mechanism from that of antibiotics. Moreover, PTT could show a similar efficient killing ability against drug-resistant bacteria [36]. Sufficient localized heat weakens the resistance of biofilms by destroying the nucleic acids, proteins, and other components comprising the biofilm, resulting in the loss of its original structure [37]. Among PTT materials, PDA has attracted great attention in biomedical applications owing to its efficient photothermal conversion ability and good biocompatibility. Previous studies have revealed that PDA can be used as antimicrobial materials such as photothermal NPs and surface coating of implants.

In this study, PDA was used as the photothermal conversion material. Zn^{2+} and D-Cys were modified on the surface of PDA NPs based on dopamine chemistry and metal coordination, which were loaded in GO hydrogel to prepare a composite hydrogel for infectious bone defect repair. GPZC can degrade and release Zn^{2+}, and the excessive Zn^{2+} could be excreted through feces and urine without any adverse effects on the human body. The primary component of GelMA is collagen, exhibiting good biocompatibility and degradability. By modifying GelMA with oxidized hyaluronic acid, a GO hydrogel with Schiff base bonds is formed, which can decompose under acidic conditions. Consequently, the GPZC hydrogel can release Zn^{2+} more rapidly in an acidic environment, endowing it with both antimicrobial and bone-enhancing properties.

It has been reported that mild heat (41–43 °C) could promote cell proliferation, wound healing and bone regeneration. Our study reveals that GPZC hydrogel enhances ALP expression and calcium deposition, elevates osteogenesis-related gene and protein expression, and remarkably enhances the osteogenic capacity after NIR irradiation. Previous studies revealed that mild thermal stimulation upregulated the

expression of heat shock proteins in cells. HSP70 enhanced the heat resistance of cells, and HSP47 facilitated the maturation of collagen I [38,39]. Both types of heat shock proteins promote the osteogenic activity of cells [40]. Several studies have indicated that HSPs, particularly HSP70, can modulate BMP signaling by interacting with components of the BMP receptor complex or by influencing the downstream SMAD signaling pathways involved in osteoblast differentiation. For example, HSP70 may assist in the stabilization of BMP receptors on the cell surface, thus enhancing BMP-mediated signaling in osteoblasts. Heat shock-induced HSPs might also interact with BMP2 or BMP7, either by enhancing their stability or promoting the expression of their target genes [41].

Heat therapy (>50 °C) effectively inhibits bacterial proliferation for infectious wound healing. However, excessive temperature (>47 °C) can cause damage to surrounding tissues, which is not conducive to tissue repair. To address this problem, two strategies were proposed in this study. Firstly, D-cysteine was modified on the surface of photothermal NPs to achieve bacteria-targeting, which results in higher local temperatures around the infected areas, thereby minimizing damage to normal tissues. Secondly, Zn^{2+} were introduced into the nanoparticle surface inspired by the "zinc finger" structure, thus enhancing the antimicrobial activity and osteogenesis [42]. Zn^{2+} has antimicrobial activity realized via oxidative stress reaction, which involves the adsorption on the surface of bacteria due to the interaction of positive and negative charges and their further penetration into bacteria [43]. Zinc finger peptides or short peptide motifs that recognize bacterial-specific ligands can be incorporated into the hydrogel to enhance bacterial adhesion or targeting, increasing the efficiency of antibacterial action by the zinc component. The zinc finger-inspired design can also potentially enhance selectivity for bacterial cells over mammalian cells, as bacteria often have specific receptors or cell wall components that can interact with the zinc finger motifs. By functionalizing the hydrogel with targeted zinc-binding peptides or using a cationic charge from Zn^{2+}, the hydrogel may exhibit preferential binding to bacterial cells rather than host cells, limiting cytotoxicity to healthy tissues. GPZ and GPZC hydrogels exhibit superior antimicrobial ability compared to GO and GP hydrogels under light-free conditions. Among these, GPZ composite hydrogels exhibit a better antibacterial effect under photothermal conditions, which could be attributed to the D-Cys on the surface hindering the release of Zn^{2+}. As shown in the results, there is potential for GPZC to influence angiogenesis. We speculated it is mainly through the release of zinc ions, which can stimulate endothelial cell proliferation, migration, and new blood vessel formation. This would improve blood supply to the infected bone site and aid in bone healing.

Bone can regenerate, repair, and restore its function [44]. However, the self-repair process of infected bone defects is slow, delayed or non-healing if not treated properly [45]. Infection can cause local or systemic inflammation, and the inflammatory response can disrupt the local microenvironment and hinder repair process [46]. Additionally, inflammatory factors, reactive oxygen species, and other bacterial-killing substances produced by immune cells are toxic to normal cells while killing bacteria [47]. Therefore, the adequate killing of bacteria at the early stage is crucial. The gross tissue view and bacterial smear plate results reveal that a large number of bacteria are visible in the Defect group, and only a small number of bacteria are visible in the GPZ + NIR and GPZC + NIR groups. Further, no bacterial growth is observed in the GPZC + NIR group during the second week, which creates a favorable pre-basic condition for bone repair. According to the results of in vitro antimicrobial experiments, the GPZ hydrogel shows better antibacterial effect than that of the GPZC hydrogel with PTT treatment. In the infected bone defects of rats, both cells and bacteria are present. And the PZC particles targeted to the bacteria, thereby showing a more efficient bactericidal effect and concurrently reducing the damage to the normal cells. This results show the function of GPZC hydrogel have spatial controllability.

At present, there are also some studies on enhancing antibacterial activity. By designing multivalent antimicrobial peptide polymers (mAMPs), the binding affinity to bacterial membranes can be enhanced, leading to a stronger antibacterial effect. This provides a new direction for the design of antimicrobial materials, particularly in the context of antibiotic-resistant bacteria, where multivalent design may serve as an effective strategy to enhance therapeutic outcomes [48]. With the rise of antibiotic resistance, the development of immunomodulatory antimicrobial biomaterials has become increasingly urgent. These materials not only kill bacteria through direct antimicrobial activity but also help clear infections by modulating immune responses, especially for chronic or refractory infections [49]. This suggests that when developing new materials, the role of the immune system should not be overlooked, particularly when addressing complex chronic infections.

NIR irradiation's effectiveness may vary depending on tissue penetration, light intensity, and the precise wavelength used, which could influence its uniformity in targeting the hydrogel material [50,51]. Additionally, bacterial targeting may not be consistent across all bacterial strains, as certain strains could have different surface properties or resistance mechanisms that affect their interaction with antibacterial materials. These factors would underscore the need for further optimization and broader evaluation across various conditions and bacterial types.

Overall, the GPZC hydrogel integrates multiple material components, significantly enhances biocompatibility, antibacterial capacity and osteogenesis ability. Compared to existing material systems, it exhibits lower toxicity to cells and tissues, thereby promoting cell adhesion and proliferation. When combined with 980 nm NIR irradiation, the GPZC hydrogel demonstrates a synergistic effect. Moderate low-temperature NIR irradiation effectively reduces secondary damage while exhibiting antibacterial and osteogenesis effects. By incorporating D-cysteine, the GPZC hydrogel not only targets infection sites more effectively to kill bacteria but also avoids the impact on normal tissues, ultimately reducing infection and inflammation.

However, studies on larger animals may provide more relevant insights into how materials perform in clinical-like conditions, since their physiology and bone structure are more similar to that of humans compared to smaller animals like rats. The work by Beagan et al. indeed provide valuable context on this topic [52]. Incorporating this perspective can also help the authors justify why their study focuses on smaller models like rats and acknowledge the limitations of these models. Recent advancements in hydrogel systems for infection control have shown great promise in combining antibacterial properties with tissue regenerative abilities [53]. These systems provide valuable insights into the design of bioactive materials, similar to the PZC hydrogel described in this study. The development of hydrogels that simultaneously address infection and bone regeneration is critical for improving clinical outcomes in infectious bone defects.

4. Conclusion

The multifunctional hydrogel developed for the treatment of infectious bone defects is an innovative approach that integrates bacteria-targeting and photothermal conversion particles. Incorporating PZC nanoparticles into the GelMA-OHA framework produces dual antibacterial and osteogenic effects facilitated via external NIR irradiation. D-Cys can take part in the metabolism of the peptidoglycan chain of bacteria, causing unintentional sterilization, denoted as "Disguise strategy". Furthermore, this D-Cys modified PDA nanoparticles could target the bacteria and selectively kill them in the infectious bone microenvironment by local temperature increase. In addition to selectively killing the bacteria, this hydrogel promotes osteogenesis by combining mild hyperthermia (42–47 °C) with Zn^{2+} release, demonstrating spatial controllability. Overall, this remarkable strategy accomplishes two critical functions of bone materials: resistance to bacteria and induction of osteogenesis. This novel strategy of accurate control regulates the

events in the microenvironment where cells and bacteria coexist, demonstrating great potential in infectious bone repair and providing insights for the repair of complex injuries with antibacterial requirements.

5. Materials and methods

5.1. Synthesis and characterizations of NPs

Dopamine hydrochloride (60 mg) was added to 100 mL of Tris base (10 mM) under vigorous stirring, followed by a 24 h reaction in the dark at room temperature. The P NPs were collected by centrifugation at 20,000 rpm for 30 min, washed thrice with Milli-Q water, and redispersed in Milli-Q water for the subsequent experiments. For preparing PZ NPs, P NPs (10 mg) were modified with Zn^{2+} by adding $ZnCl_2$ (10 mg/mL, 0.2 mL) in acid buffer (10 mL, pH = 5.5). After 5 h, PZ were separated via centrifugation, washed with water, and dried for further use. For the preparation of PZC NPs, PZ were labeled with D-Cys by adding D-Cys powder (10 mg) in Milli-Q water. After 5 h, D-Cys Zn^{2+} -modified PDA NPs were separated via centrifugation, washed with water, and dried for further use. FTIR (Nicolet iS5, Thermo, US) was used to characterize the synthesized PZC. The ζ-potential and dynamic size of PDAs were measured using Zetasizer Nano 90 (Malvern). The particles were observed using TEM (FEI, USA) at an acceleration voltage of 120 kV. The morphology of composite hydrogels was observed by SEM, Quanta 250, America. The mechanical properties of composite hydrogels were evaluated using a universal material testing machine (Shanghai Hengyi, China).

5.2. Preparation of the composite hydrogels

To synthesize HA-CHO, 1.5 g of hyaluronic acid (HA) was dissolved in 150 mL of deionized water. Subsequently, 802 mg of sodium periodate was added, and the mixture was stirred for 2 h. The reaction was quenched by the addition of 200 μL of ethylene glycol, and the solution was dialyzed in deionized water to remove excess reagents. The HA-CHO product was then freeze-dried and stored at 4 °C for future use.

For the preparation of the composite hydrogel, 1 g of G sponge, 50 mg of the photoinitiator lithium phenyl-2,4,6-trimethyl-benzoyl phosphinate, and 100 mg of HA-CHO were dissolved in 20 mL of deionized water at 37 °C. Following this, 40 mg of P, PZ, or PZC was added to the solution, which was then stirred thoroughly to ensure uniform dispersion. The final composite hydrogel (designated as GP, GPZ, or GPZC) was obtained after UV light crosslinking (405 nm). The concentration of GO, GP, GPZ, and GPZC in the hydrogel is 2 mg/mL.

5.3. Photothermal performance test

A machine (model: KS-810F-8000, manufacturer: Kai Site Electronic Technology, China) were used as the light emitting source (wavelength: 980 nm). The temperature of the samples was tracked in real time with the help of TI27 infrared thermal imager produced by Fluke Company. The samples were placed in a 24 well culture plate and then irradiated with NIR light for 10 min. Next, the near-infrared light source was switched off for 18 min. The temperature is monitored immediately every minute. This procedure was repeated thrice.

5.4. Cell morphology and cell viability

BMSCs were incubated with different hydrogels for one day. After that, the cells were fixed with 2.5 % glutaraldehyde solution for half an hour. Then the cells were stained by phalloidin and DAPI for F-actin and nuclei respectively. Cell proliferation was determined by CCK-8 assay. For this determination, 1.0×10^3 BMSCs were seeded on the hydrogels and further cultured 1, 3, and 5 days. At different time points, CCK -8 reagent was added into culture medium and the cells were cultured for 2 h for detection. CCK-8 reagent manufactured by Dojindo Corporation, Japan, and the absorbance was used for CCK-8 measurement at a wavelength of 450 nm.

5.5. In vitro release of Zn^{2+} and D-cys from the hydrogels

The GPZ and GPZC composite hydrogels were soaked in 5 mL PBS solution with pH 7.2 and 5.5, respectively. These samples were incubated in an oven at 37 °C, and the buffer was aspirated at 2 h, and 1, 2, 3, 4, 5, 6, 7, 9, 11, 14, and 21 days, and 5 mL of fresh buffer was added. Finally, the released Zn^{2+} and D-Cys were detected using zinc ion and D-cys assay kits, respectively.

5.6. Live/dead cell staining

Cell viability was assessed by quantitative analysis using calcein-am/PI (Dojindo, Japan). The cells were washed three times with PBS, and then incubated with 2 μM calcein-am and 4 μM propidium iodide (PI) for 15 min at 37 °C in the dark. Subsequently, living cells and dead cells were observed by a fluorescence microscope (Olympus IX71, Tokyo, Japan).

5.7. Detection of in vitro antibacterial property

The inhibitory efficiency of hydrogel on bacterial biofilm was detected. After coculturing with *S. aureus*, the hydrogel was washed with PBS for three times, and then fixed with 95 % ethanol at room temperature for 40 min. Then, *S. aureus* was stained by AO/EB reagent, and images were collected by inverted fluorescence microscope. Subsequently, we conducted an antimicrobial test to determine the antimicrobial efficacy of the hydrogels. For this experiment, the hydrogel was placed in the center of an LB agar medium containing 100 μL bacterial suspension. A suspension of *S. aureus* containing 10^6 to 10^7 colony-forming units per mL was incubated at 37 °C for 18 h. After that, quantitative analysis was performed to evaluate the antibacterial ability of the hydrogels. The hydrogels were immersed in PBS containing *S. aureus*. Supernatants were collected at different time points and added into LB gel plates to monitor the growth of the bacteria. Subsequently, the number of bacterial colony was counted with the help of ImageJ. The *S. aureus* was cultured and allowed to grow 1 day on hydrogels. Thereafter, the samples were washed and fixed. After gradient dehydration and critical point drying, the sample was observed by SEM. For anti-biofilm activity, 200 μL of *S. aureus* suspension (10^7 CFU mL^{-1}) was added dropwise into 24-well plates, followed by the addition of 500 μL of LB liquid medium. After 6 h, the composite hydrogel was added to the plates, irradiated using 980 nm NIR light for 10 min, and then placed into a 37 °C, 5 % CO_2 incubator. After 24 h, the biofilm on the bottom of the plates was stained with a crystal violet staining solution, and microscopy was used to observe the biofilm formation. After that, 95 % ethanol was added to dissolve the biofilm, and the absorbance was measured at 590 nm.

Antimicrobial rate (%) = (number of colonies in the control group - number of colonies in the experimental group)/number of colonies in control group × 100%

5.8. Characterizations of bacteria-targeting performance

BMSCs, *S. aureus,* and PZC were stained and labeled with DiO (excitation wavelength: 484 nm), DiI (excitation wavelength: 549 nm), and Cy5 (excitation wavelength: 650 nm), respectively. The stained BMSCs and *S. aureus* were simultaneously cocultured in plates at a 20: 1 ratio (1×10^5 cells and 5×10^3 bacteria per well). After 2 h, the stained PZC NPs were added to the plates, 1 mL of medium (80 % α-MEM

complete medium and 20 % LB medium) was added to each well, and the plates were incubated in a 5 % CO_2 incubator at 37 °C. After that, the cell and bacterial growth status and the location of the particles were observed using laser scanning confocal microscopy.

5.9. Evaluation of in vitro osteogenesis property

BMSC cells were seeded in six-well plates (1×10^5 cells/well). After one day, the medium was replaced with osteogenic induction medium containing 10 mM β-glycerophosphate, 10 nM dexamethasone and 50 mM L-ascorbic acid 2-phosphate. The hydrogels are placed in the plates. After 7 days of culture, cells were stained using BCIP/NBT kit (Beyotime, China) for ALP staining after fixation with 4 % formaldehyde for 20 min, and observed by a microscope. After 21 days of culture, the mineralized knot was quantitatively evaluated. During this process, a 10 % cetylpyridinium chloride solution was added to the samples and the absorbance of the solution was measured at 425 nm.

5.10. Quantitative reverse-transcription polymerase chain reaction (qRT-PCR) analysis

BMSCs (1×10^5 cells/well) in different groups were incubated for 7 and 21 days. Then, the total RNA in BMSC was extracted by Trizol reagent (Invitrogen, Carlsbad, USA), and the miRNA was separated by the exosome RNA purification kit produced by Qiagen, Germany. After that, that obtained RNA sample were subjected to a reverse transcription process using an AcDNA synthesis kit (Takara, Japan), followed by a real-time quantitative reverse transcription-polymerase chain reaction using a Miscript SYBR Green PCR kit (Qiagen, Inc.). The primer sequences used in this study is shown in Table 1.

5.11. Western blot analysis

Proteins were extracted from the cells and were purified by centrifugation. Then, the concentration of proteins was determined using a BCA kit. The protein samples were loaded into a polyacrylamide gel for electrophoresis. Subsequently, the proteins in the gel were transferred to a PVDF film. Non-specific binding sites on the film were closed with a Western blot closure solution to reduce the background signal. The film was incubated with specific primary antibodies (GAPDH, RUNX2, ALP, COL1, and OCN) and later washed with buffer to remove unbound antibodies. The film was incubated with horseradish peroxidase (HRP)-labeled secondary antibodies, followed by washing the unbound secondary antibodies. Finally, a drop of the mixed ECL reagent was added to the membrane to cover it, which was scanned and developed using a WB developer.

5.12. Animal studies

The protocols were authorized by the Soochow University of China's Institutional Animal Care and Use Committee by following Chinese national standards for the care and use of experimental animals (SUDA20220711A09). The Sprague-Dawley (SD) rats (300–350 g) were used to construct an infectious femoral condyle defect model. Pentobarbital sodium (30 mg/kg, Sigma-Aldrich) was applied to induce anesthesia, and the rats' hindlimbs were shaved and sterilized using povidone-iodine. After blunt dissection, the femur was exposed, and a bone drill was used to create bone defects (deepth: 3 mm; diameter: 3 mm) on the femoral condyles. *S. aureus* (10^7 CFU/mL) was injected into the hollow of the femur condyle. The composite hydrogels were exposed to blue light (405 nm) for 30 s after their injection into the femoral condyle cavity. After 4 and 8 weeks, animals are euthanized and the femurs were removed and preserved with 4 % paraformaldehyde.

Table 1
qPCR primer sequences.

Gene Name	Forward (5′-3′)	Reversed (5′-3′)
Alpl	TATGTCTGGAACCGCACTGAAC	CACTAGCAAGAAGAAGCCTTTGG
Runx2	ATCCAGCCACCTTCACTTACACC	GGGACCATTGGGAACTGATAGG
Col1a1	CAGGCTGGTGTGATGGGATT	CCAAGGTCTCCAGGAACACC
Bglap	AACGGTGGTGCCATAGATGC	AGGACCCTCTCTCTGCTCAC
Gapdh	GACATGCCGCCTGGAGAAAC	AGCCCAGGATGCCCTTTAGT

5.13. Micro-CT analysis

A micro-CT system (SkyScan 1176, Bruker, Germany) was used to scan and analyze the samples. CT-Vox software was used to reconstruct 3D images for further analysis. Several parameters, including BV, BV/TV, Trabecular thickness (Tb. Th), Trabecular number (Tb. N), and Trabecular separation (Tb.Sp), were analyzed.

5.14. Histomorphological analysis

Decalcification procedures of the samples were performed using EDTA decalcification solution. The decalcification solution was changed every four days until the bone was completely decalcified. In addition, the newly formed trabecular structure was observed by H&E and Masson staining. The images were captured using a Nikon H600L optical microscope (from Tokyo, Japan).

5.15. In vivo antibacterial ability

In order to explore its *in vivo* antibacterial ability, the GP, GPZ and GPZC hydrogels containing 1.0×10^7 CFU mL^{-1} *S. aureus* were implanted into the bone defects of rats. The bacterial infection after NIR irradiation was observed. After the implantation action, a series of care measures were carried out on the area. Specifically, 1 and 2 week after surgery, NIR irradiation (980 nm, 1.0 W, 6 min) were carried out. When collecting samples, long bones were extracted from rats and placed in PBS. We then evaluated the antibacterial performance through bacterial coating experiments.

5.16. Statistical analysis

The metric results for the data set are presented as a combination (SD) of the mean and its standard deviation (SD). In order to test the difference between different groups, we used the single factor analysis of variance (ANOVA) combined with Tukey's HSD test to compare multiple groups; for the comparison of only two groups, we used the independent sample *t*-test method.Data analysis was performed using GraphPad Prism 8 (La Jolla, CA, USA) software. A p value of less than 0.05 was used as a criterion for a statistically significant difference. Each experiment was validated in at least three independent replicates.

CRediT authorship contribution statement

Kexin Li: Writing – original draft, Methodology, Investigation, Data curation, Conceptualization. **En Xie:** Methodology, Investigation, Data curation. **Chengyuan Liu:** Software, Methodology, Formal analysis. **Jie Hu:** Visualization, Software, Methodology. **Qianglong Chen:** Software, Methodology, Formal analysis. **Jiaying Li:** Methodology, Investigation. **Huan Wang:** Software, Methodology. **Qingchen Meng:** Visualization, Software. **Dachuan Liu:** Visualization. **Bin Meng:** Resources, Methodology. **Ting Liang:** Methodology, Investigation. **Jinjin Ma:** Methodology. **Zhangqin Yuan:** Methodology. **Lijie Wang:** Software. **Wenmiao Shu:** Methodology. **Haijiao Mao:** Resources. **Fengxuan Han:** Writing – review & editing, Validation, Project administration, Conceptualization. **Bin Li:** Writing – review & editing, Project administration, Conceptualization.

Ethics approval and consent to participate

The animal experiments and protocols were authorized by the Soochow University of China's Institutional Animal Care and Use Committee by following Chinese national standards for the care and use of experimental animals (SUDA20220711A09).

Declaration of competing interest

The authors declare the following personal relationships which may be considered as potential competing interests: Lijie Wang is currently employed by Sanitation & Environment Technology Institute of Soochow University Ltd.

Acknowledgements

K.L. and E.X. contributed equally to this work. The authors are grateful for the funding provided for this study by the National Key R&D Program of China (2023YFB3810200, 2023YFB3810201), the National Natural Science Foundation of China (81925027, 32171350, 32471410), International Cooperation Project of Ningbo City (2023H013), Jiangsu Basic Research Program (Natural Science Foundation) (BK20240020), Medical and Health Science and Technology Innovation Project of Suzhou (SKY2022105), Jiangsu Province Science and Technology Plan Special Fund (BE2022730), Postdoctoral Fellowship Program of CPSF (BX20230253, GZB20230505), Basic cutting-edge innovation cross project of Suzhou Medical College of Soochow University (YXY2302010, YXY2304046, YXY2304053), the China Postdoctoral Science Foundation under Grant Number 2023TQ0235, Science and Technology Development Project of Suzhou (SGC202379, SZS2023043) and the Priority Academic Program Development (PAPD) of Jiangsu Higher Education Institutions.

Appendix A. Supplementary data

Supplementary data to this article can be found online at https://doi.org/10.1016/j.bioactmat.2025.02.002.

References

[1] E.A. Masters, B.F. Ricciardi, K.L.M. Bentley, T.F. Moriarty, E.M. Schwarz, G. Muthukrishnan, Skeletal infections: microbial pathogenesis, immunity and clinical management, Nat. Rev. Microbiol. 20 (7) (2022) 385–400.
[2] S. Baertl, W.J. Metsemakers, M. Morgenstern, V. Alt, R.G. Richards, T.F. Moriarty, K. Young, Fracture-related infection, Bone Joint Res 10 (6) (2021) 351–353.
[3] D.G.J. Larsson, C.F. Flach, Antibiotic resistance in the environment, Nat. Rev. Microbiol. 20 (5) (2022) 257–269.
[4] J.M. Sadowska, K.J. Genoud, D.J. Kelly, F.J. O'Brien, Bone biomaterials for overcoming antimicrobial resistance: advances in non-antibiotic antimicrobial approaches for regeneration of infected osseous tissue, Mater. Today 46 (2021) 136–154.
[5] W. Wang, K.W.K. Yeung, Bone grafts and biomaterials substitutes for bone defect repair: a review, Bioact. Mater. 2 (4) (2017) 224–247.
[6] Y. Fan, H. Ran, Z. Wang, C. Ning, J. Zhai, P. Yu, Semiconductive biomaterials for pathological bone repair and regeneration, Adv. Funct. Mater. (2024) 2308310.
[7] J.M.V. Makabenta, A. Nabawy, C.H. Li, S. Schmidt-Malan, R. Patel, V.M. Rotello, Nanomaterial-based therapeutics for antibiotic-resistant bacterial infections, Nat. Rev. Microbiol. 19 (1) (2021) 23–36.
[8] Y.Z. Wu, D.Z. Xiao, P. Liu, Q. Liao, Q.D. Ruan, C. Huang, L.L. Liu, D. Li, X.L. Zhang, W. Li, K.W. Tang, Z.W. Wu, G.M. Wang, H.Y. Wang, P.K. Chu, Nanostructured conductive polypyrrole for antibacterial components in flexible wearable devices, Research 6 (2023) 74.
[9] C.X. Shu, W. Zhang, Y.W. Zhang, Y. Li, X.B. Xu, Y.N. Zhou, Y. Zhang, Q. Zhong, C. He, Y. Zhu, X.L. Wang, Copper-bearing metal-organic framework with mucus-penetrating function for the multi-effective clearance of mucosalcolonized helicobacter pylori, Research 7 (2024) 358.
[10] Y. Yan, Y. Li, Z. Zhang, X. Wang, Y. Niu, S. Zhang, W. Xu, C. Ren, Advances of peptides for antibacterial applications, Colloid Surface B: Biointerfaces 202 (2021) 111682.
[11] Z. Shu, C. Zhang, L. Yan, H. Lei, C. Peng, S. Liu, L. Fan, Y. Chu, Antibacterial and osteoconductive polycaprolactone/polylactic acid/nano-hydroxyapatite/Cu@ZIF-8 GBR membrane with asymmetric porous structure, Int. J. Biol. Macromol. 224 (2023) 1040–1051.
[12] V.M. Schatkoski, T. Larissa do Amaral Montanheiro, B.R. Canuto de Menezes, R. M. Pereira, K.F. Rodrigues, R.G. Ribas, D. Morais da Silva, G.P. Thim, Current advances concerning the most cited metal ions doped bioceramics and silicate-based bioactive glasses for bone tissue engineering, Ceram. Int. 47 (3) (2021) 2999–3012.
[13] S. Rashki, K. Asgarpour, H. Tarrahimofrad, M. Hashemipour, M.S. Ebrahimi, H. Fathizadeh, A. Khorshidi, H. Khan, Z. Marzhoseyni, M. Salavati-Niasari, H. Mirzaei, Chitosan-based nanoparticles against bacterial infections, Carbohydr. Polym. 251 (2021) 117108.
[14] W. Meng, Z. Lin, X. Cheng, S. Gou, R. Wang, P. Bu, Y. Li, B. Mi, Y. Yu, Q. Feng, K. Cai, Thiourea-cation chelation based hydrogel and its application as antibacterial dressing for the repair of diabetic wound, Adv. Funct. Mater. 34 (22) (2024) 2314202.
[15] M. Godoy-Gallardo, U. Eckhard, L.M. Delgado, Y.J.D. de Roo Puente, M. Hoyos-Nogués, F.J. Gil, R.A. Perez, Antibacterial approaches in tissue engineering using metal ions and nanoparticles: from mechanisms to applications, Bioact. Mater. 6 (12) (2021) 4470–4490.
[16] G. Qing, X. Zhao, N. Gong, J. Chen, X. Li, Y. Gan, Y. Wang, Z. Zhang, Y. Zhang, W. Guo, Y. Luo, X.J. Liang, Thermo-responsive triple-function nanotransporter for efficient chemo-photothermal therapy of multidrug-resistant bacterial infection, Nat. Commun. 10 (1) (2019) 4336.
[17] Y. Wu, W. Zhou, L. Zhou, S.-I. In, J. Lei, L. Wang, J. Zhang, Y. Liu, Near-infrared photothermal effect enhanced heterogeneous catalysis of Co_3O_4/PDA composite for highly efficient activation of peroxymonosulfate to degrade antibiotic pollutants, Chem. Eng. J. 474 (2023) 145267.
[18] X. Bao, J. Zhao, J. Sun, M. Hu, X. Yang, Polydopamine nanoparticles as efficient scavengers for reactive oxygen species in periodontal disease, ACS Nano 12 (9) (2018) 8882–8892.
[19] M. Wu, H. Liu, D. Li, Y. Zhu, P. Wu, Z. Chen, F. Chen, Y. Chen, Z. Deng, L. Cai, Smart-responsive multifunctional therapeutic system for improved regenerative microenvironment and accelerated bone regeneration via mild photothermal therapy, Adv. Sci. 11 (2) (2024) e2304641.
[20] F. Zhang, J. Zhuang, Z. Li, H. Gong, B.E. de Ávila, Y. Duan, Q. Zhang, J. Zhou, L. Yin, E. Karshalev, W. Gao, V. Nizet, R.H. Fang, L. Zhang, J. Wang, Nanoparticle-modified microrobots for in vivo antibiotic delivery to treat acute bacterial pneumonia, Nat. Mater. 21 (11) (2022) 1324–1332.
[21] B. Li, P. Thebault, B. Labat, G. Ladam, V. Alt, M. Rupp, C. Brochausen, J. Jantsch, M. Ip, N. Zhang, W.-H. Cheung, S.Y.S. Leung, R.M.Y. Wong, Implants coating strategies for antibacterial treatment in fracture and defect models: a systematic review of animal studies, J Orthop Transl 45 (2024) 24–35.
[22] Y.P. Hsu, E. Hall, G. Booher, B. Murphy, A.D. Radkov, J. Yablonowski, C. Mulcahey, L. Alvarez, F. Cava, Y.V. Brun, E. Kuru, M.S. VanNieuwenhze, Fluorogenic D-amino acids enable real-time monitoring of peptidoglycan biosynthesis and high-throughput transpeptidation assays, Nat. Chem. 11 (4) (2019) 335–341.
[23] M. Chen, S. Zhang, Z. He, Controlled block polypeptide composed of D-type amino acids: a therapeutics delivery platform to inhibit biofilm formation of drug-resistant bacteria, ACS Appl. Bio Mater. 3 (9) (2020) 6343–6350.
[24] C. Yang, L. Chu, Y. Zhang, Y. Shi, J. Liu, Q. Liu, S. Fan, Z. Yang, D. Ding, D. Kong, J. Liu, Dynamic biostability, biodistribution, and toxicity of L/D-peptide-based supramolecular nanofibers, ACS Appl. Mater. Interfaces 7 (4) (2015) 2735–2744.
[25] F. Zhao, A. Gao, Q. Liao, Y. Li, I. Ullah, Y. Zhao, X. Ren, L. Tong, X. Li, Y. Zheng, P. K. Chu, H. Wang, Balancing the anti-bacterial and pro-osteogenic properties of Ti-based implants by partial conversion of ZnO nanorods into hybrid Zinc phosphate nanostructures, Adv. Funct. Mater. 34 (17) (2024) 2311812.
[26] B. Chen, P. Yu, W.N. Chan, F. Xie, Y. Zhang, L. Liang, K.T. Leung, K.W. Lo, J. Yu, G. M.K. Tse, W. Kang, K.F. To, Cellular zinc metabolism and zinc signaling: from biological functions to diseases and therapeutic targets, Signal Transduct. Targeted Ther. 9 (1) (2024) 6.
[27] S. Duan, R. Wu, Y.-H. Xiong, H.-M. Ren, C. Lei, Y.-Q. Zhao, X.-Y. Zhang, F.-J. Xu, Multifunctional antimicrobial materials: from rational design to biomedical applications, Prog. Mater. Sci. 125 (2022) 100887.
[28] X. Zhang, R.M. Blumenthal, X. Cheng, Updated understanding of the protein-DNA recognition code used by C2H2 zinc finger proteins, Curr. Opin. Struct. Biol. 87 (2024) 102836.
[29] D. Neuhaus, Zinc finger structure determination by NMR: why zinc fingers can be a handful, Prog. Nucl. Magn. Reson. Spectrosc. 130–131 (2022) 62–105.
[30] S. Uyttebroek, B. Chen, J. Onsea, F. Ruythooren, Y. Debaveye, D. Devolder, I. Spriet, M. Depypere, J. Wagemans, R. Lavigne, J.P. Pirnay, M. Merabishvili, P. De Munter, W.E. Peetermans, L. Dupont, L. Van Gerven, W.J. Metsemakers, Safety and efficacy of phage therapy in difficult-to-treat infections: a systematic review, Lancet Infect. Dis. 22 (8) (2022) e208–e220.
[31] Y. Shen, H. Wang, H. Xie, J. Zhang, Q. Ma, S. Wang, P. Yuan, H. Xue, H. Hong, S. Fan, W. Xu, Z. Xie, L-arginine promotes angio-osteogenesis to enhance oxidative stress-inhibited bone formation by ameliorating mitophagy, J Orthop Transl 46 (2024) 53–64.
[32] L. He, D. Di, X. Chu, X. Liu, Z. Wang, J. Lu, S. Wang, Q. Zhao, Photothermal antibacterial materials to promote wound healing, J. Contr. Release 363 (2023) 180–200.
[33] D. Xu, Z. Li, L. Li, J. Wang, Insights into the photothermal conversion of 2D MXene nanomaterials: synthesis, mechanism, and applications, Adv. Funct. Mater. 30 (47) (2020) 2000712.
[34] O. Shelonchik, N. Lemcoff, R. Shimoni, A. Biswas, E. Yehezkel, D. Yesodi, I. Hod, Y. Weizmann, Light-induced MOF synthesis enabling composite photothermal materials, Nat. Commun. 15 (1) (2024) 1154.

[35] W. Xiaodan, L. Qinmei, Y. Huawei, Effect of radiation sterilisation on the structure and antibacterial properties of antimicrobial peptides, Biomater Transl 4 (1) (2023) 51–61.
[36] Z. Zeng, Y. Li, K. Deng, D. Zou, L. Liu, B. Guo, Y. Liu, C. Shen, X. Liang, X. Xu, Thermal-cascade multifunctional therapeutic systems for remotely controlled synergistic treatment of drug-resistant bacterial infections, Adv. Funct. Mater. (2024) 2311315.
[37] O. Ciofu, C. Moser, P. Jensen, N. Høiby, Tolerance and resistance of microbial biofilms, Nat. Rev. Microbiol. 20 (10) (2022) 621–635.
[38] Z. Yu, H. Wang, B. Ying, X. Mei, D. Zeng, S. Liu, W. Qu, X. Pan, S. Pu, R. Li, Y. Qin, Mild photothermal therapy assist in promoting bone repair: related mechanism and materials, Mater Today Bio 23 (2023) 100834.
[39] X. Yi, Q.Y. Duan, F.G. Wu, Low-temperature photothermal therapy: strategies and applications, Research (2021) 9816594, 2021.
[40] Y. Wang, X. Hu, L. Zhang, C. Zhu, J. Wang, Y. Li, Y. Wang, C. Wang, Y. Zhang, Q. Yuan, Bioinspired extracellular vesicles embedded with black phosphorus for molecular recognition-guided biomineralization, Nat. Commun. 10 (1) (2019) 2829.
[41] Z. Zhang, Y. Ma, S. Guo, Y. He, G. Bai, W. Zhang, Low-intensity pulsed ultrasound stimulation facilitates in vitro osteogenic differentiation of human adipose-derived stem cells via up-regulation of heat shock protein (HSP)70, HSP90, and bone morphogenetic protein (BMP) signaling pathway, Biosci. Rep. 38 (3) (2018) BSR20180087.
[42] Y. Jin, F. Kanwal, Z. Xiaojun, H. Chuanglong, Meticulously engineered three-dimensional-printed scaffold with microarchitecture and controlled peptide release for enhanced bone regeneration, Biomater Transl 5 (1) (2024) 69–83.
[43] A. Frei, A.D. Verderosa, A.G. Elliott, J. Zuegg, M.A.T. Blaskovich, Metals to combat antimicrobial resistance, Nat. Rev. Chem 7 (3) (2023) 202–224.
[44] G. Zhu, T. Zhang, M. Chen, K. Yao, X. Huang, B. Zhang, Y. Li, J. Liu, Y. Wang, Z. Zhao, Bone physiological microenvironment and healing mechanism: basis for future bone-tissue engineering scaffolds, Bioact. Mater. 6 (11) (2021) 4110–4140.
[45] Z. Cao, Z. Qin, G.J. Duns, Z. Huang, Y. Chen, S. Wang, R. Deng, L. Nie, X. Luo, Repair of infected bone defects with hydrogel materials, Polymers 16 (2) (2024) 281.
[46] J.L. Casanova, L. Abel, Mechanisms of viral inflammation and disease in humans, Science 374 (6571) (2021) 1080–1086.
[47] H. Sies, V.V. Belousov, N.S. Chandel, M.J. Davies, D.P. Jones, G.E. Mann, M. P. Murphy, M. Yamamoto, C. Winterbourn, Defining roles of specific reactive oxygen species (ROS) in cell biology and physiology, Nat. Rev. Mol. Cell Biol. 23 (7) (2022) 499–515.
[48] X. Chen, X. Li, W. He, M. Wang, A. Gao, L. Tong, S. Guo, H. Wang, G. Pan, Rational multivalency construction enables bactericidal effect amplification and dynamic biomaterial design, Innovation 4 (5) (2023) 100483.
[49] S. Zhang, H. Yang, M. Wang, D. Mantovani, K. Yang, F. Witte, L. Tan, B. Yue, X. Qu, Immunomodulatory biomaterials against bacterial infections: progress, challenges, and future perspectives, Innovation 4 (6) (2023) 100503.
[50] W. Pan, B. Wu, C. Nie, T. Luo, Z. Song, J. Lv, Y. Tan, C. Liu, M. Zhong, T. Liao, Z. Wang, G. Yi, L. Zhang, X. Liu, B. Li, J. Chen, L. Zheng, NIR-II responsive nanohybrids incorporating thermosensitive hydrogel as sprayable dressing for multidrug-resistant-bacteria infected wound management, ACS Nano 17 (12) (2023) 11253–11267.
[51] S. Xue, X. Zhou, W. Sang, C. Wang, H. Lu, Y. Xu, Y. Zhong, L. Zhu, C. He, J. Ma, Cartilage-targeting peptide-modified dual-drug delivery nanoplatform with NIR laser response for osteoarthritis therapy, Bioact. Mater. 6 (8) (2021) 2372–2389.
[52] M.L.C. Beagan, C.H. Dreyer, L.K. Jensen, H.E. Jensen, T.E. Andersen, S. Overgaard, M. Ding, The potential of sheep in preclinical models for bone infection research - a systematic review, J Orthop Transl 45 (2024) 120–131.
[53] J. Guo, H. Yao, X. Li, L. Chang, Z. Wang, W. Zhu, Y. Su, L. Qin, J. Xu, Advanced hydrogel systems for mandibular reconstruction, Bioact. Mater. 21 (2023) 175–193.